# Pre-launch calibration and validation of the Airborne Hyper-Angular Rainbow Polarimeter (AirHARP) instrument

Brent A. McBride[2,3], J. Vanderlei Martins[1,2], J. Dominik Cieslak[1,2], Roberto Fernandez-Borda[1,2], Anin Puthukkudy[1,2], Xiaoguang Xu[1,2], Noah Sienkiewicz[1,2], Brian Cairns[4], and Henrique M. J. Barbosa[1]

5 [1]Department of Physics, University of Maryland, Baltimore County, MD, USA
[2]Earth and Space Institute, University of Maryland, Baltimore County, Baltimore, MD, USA
[3]Science Systems and Applications, Inc., Lanham, MD, USA
[4]NASA Goddard Institute for Space Studies, New York, NY, USA

*Correspondence to*: Brent A. McBride (mcbride1@umbc.edu)

10 **Abstract.** The Airborne Hyper-Angular Rainbow Polarimeter (AirHARP) is a new imaging polarimeter instrument, capable of sampling a single Earth target from up to 120 viewing angles, in four spectral channels, and three linear polarization states across a 114° field of view (FOV). AirHARP is telecentric in the image space and simultaneously images three linear polarization states with no moving parts. These two aspects of the design allow for a simple and efficient quantitative calibration. Using coefficients 15 derived at the center of the lens and the detector flatfields, we can calibrate the entire AirHARP sensor in a variety of lab, field, and space environments. We show that this telecentric calibration technique yields a one sigma absolute uncertainty of 0.25% in degree of linear polarization (DOLP) in the lab for all channels and for pixels around the optical axis. To validate across the FOV, we compare our multi-angle reflectance and polarization data with the Research Scanning Polarimeter (RSP) over targets sampled 20 during the NASA Aerosol Characterization from Polarimeter and Lidar (ACEPOL) campaign. We use the error-normalized difference technique to estimate how well the instruments compare relative to their error models. We find that AirHARP and RSP reasonably agree for reflectance and DOLP within two standard deviations of their mutual uncertainty at 550, 670, and 870 nm, and over a limited set of ocean and desert scenes. This calibration technique makes the HARP design attractive for new spaceborne 25 climate missions: HARP CubeSat (2020-2022),  HARP2 (2024-) on the NASA Plankton-Aerosol-Cloud-ocean Ecosystem (PACE), and beyond.

# 1 Introduction

Aerosols and their effect on clouds are one of our largest climate challenges. These particles are difficult to model and measure from satellite. Some aerosols are irregularly shaped, absorbing, and dimly reflecting, and others are spherical and efficient at scattering sunlight. They are transported across the globe from a variety of source regions, perturb the boundary layer, and interact with clouds in different ways depending on their location in the atmosphere and composition. Aerosols can control how long clouds last, how bright they are, and when they will precipitate (Boucher et al. 2013). This complexity makes it difficult to estimate the impacts of clouds and aerosols on our climate system. However, this uncertainty drives innovation and instrument development. Satellite measurements with a range of spectral, angular, spatial, and polarized capabilities can improve how we measure these properties at global scales (NASA 2018). Instruments that combine these features, called multi-angle polarimeters (MAPs), may make considerable enhancements to our climate record in this direction (Dubovik et al. 2019). They are highly compatible with current instruments, expand the information content possible in a single measurement, and can be designed to small and cost-effective form factors. Recent studies show that microphysical retrievals done on multi-angle polarimetric (MAP) data are highly attractive for future missions and improving our knowledge of microphysical properties (Mishchenko et al. 2004, Knobelspiesse et al. 2012, Stamnes et al. 2018, Remer et al. 2019). Of these, those that sample with less than or equal to 3% relative uncertainty in absolute radiometric calibration and 0.5% absolute uncertainty in *degree of linear polarization* (DOLP) are optimal (NASA 2015, NASA 2021).

Over the past decade, several research teams have demonstrated a variety of effective MAP designs in aircraft campaigns and lab calibrations. Prominent MAP instruments include the Research Scanning Polarimeter (RSP, Cairns et al. 1999), the SPEX (Hasekamp et al. 2019), Airborne Multi-angle Spectro-Polarimetric Imager (AirMSPI, Diner et al. 2013), the MAP on specMACS (Weber et al. 2024), and the Hyper-Angular Rainbow Polarimeter (HARP, Martins et al. 2018). The RSP is a 14mrad single-pixel scanner that measures polarized radiation from a target pixel at up to 150+ viewing angles. The RSP measures these angles across nine spectral channels from 410-2200nm. Its narrow viewing angle density (0.8°), together with high polarimetric uncertainty (~0.002 in DOLP), allows for a near-seamless reconstruction of the scattering profile of any ground target. RSP measurements paved the way for new

55  cloud and ice property retrievals (Sinclair et al. 2021, van Diedehoven et al. 2013), ocean color (Chowdhary et al. 2012), and improved cross-comparisons with other instruments (Knobelspiesse et al. 2019, van Harten et al. 2018, Smit et al. 2019). The RSP represents one possible MAP design but there are others that take advantage of spectral information and modulation of the polarized signal. The SPEX instrument is a hyperspectral multi-angle polarimeter capable of measuring a ground target from five to

60  nine viewing angles over 109 spectral channels (400-800nm). SPEX selects wavelengths using an internal diffraction grating and uses spectral modulation to de-convolve total radiance and DOLP signals from the measurements. SPEX measurements may narrow uncertainty in aerosol microphysical retrievals of single scattering albedo, size, shape, and refractive indices, beyond the capabilities of current space platforms (Hasekamp and Landgraf 2007, Hasekamp 2019). Also, highly accurate (~0.002 in DOLP), SPEX was

65  one of the polarimeters contributed to the NASA PACE mission specifically for new aerosol science (Werdell et al. 2019, Rietjens et al. 2019). The AirMSPI instrument measures the incident polarization state of a target using photoelastic modulation (Diner et al. 2013). AirMSPI tracks the same point on the ground with a programmable gimble that locks into specific view angles (*step-and-stare*). In a separate sampling mode, MSPI scans a pushbroom FPA over a wide range of scattering angles (*continuous sweep*).

70  The MSPI concept was optimized into the Multi-Angle Imager for Aerosols (MAIA), a space mission that will characterize air pollution over city targets (Diner et al. 2018). The AirMSPI team reports <0.005 DOLP uncertainty for all spectral channels, which is achieved and further improved by aggregating pixels (van Harten and Diner, 2015, van Harten et al. 2018, Knobelspiesse et al. 2019). Finally, the MAP on specMACS is a dual-camera, wide FOV sensor with a division-of-focal-plane polarimetric design and a

75  three-band visible Bayer filter on each detector. Both cameras are positioned symmetrically off-nadir, such that both FOVs overlap for some pixels and contain unique spatial coverage ion others. The angular density is the sharpest of any MAP (0.3°), which has been recently demonstrated in high resolution cloud retrieval studies (Pörtge et al. 2023).

This paper discusses the HARP, a wide field, Earth-observing modern MAP that is capable of

80  highly-resolved, highly-accurate climate measurements. This work focuses on AirHARP, the aircraft version of the HARP design. This work will discuss the optics of the instrument, how it combines the strengths of the above instruments, and how our calibration process maintains high measurement accuracy

in lab and in the field. In this paper, we introduce the AirHARP instrument (Section 2), step through the full quantitative calibration process in detail (Section 3), and discuss validation studies done in the lab

85 and on flight data (Section 4). We close in Section 5 with a discussion of limitations and look ahead to the HARP CubeSat satellite payload and the HARP2 deployment on-board the NASA PACE mission in 2023.

## 2 The Airborne Hyper-Angular Rainbow Polarimeter (AirHARP)

The AirHARP instrument is a wide field-of-view imaging polarimeter, shown in Figure 1.

90 AirHARP samples Earth targets at four optical channels: 440 (14), 550 (12), 670 (18), and 870 (37) nm. These four channels are selected passively using a custom stripe filter on top of a charge-coupled device (CCD) detector FPA. The stripe filter distributes the four AirHARP channels across 120 distinct regions of the detector, called *view sectors*. The 670nm band covers 60 of these view sectors and the other 60 are split equally across the other three bands. AirHARP contains three CCD detectors that each image a

95 component of the incident beam through the optical path. Each detector is covered by a linear polarizer, set at a unique angle. This design decouples the incident polarization into orthogonal S-and P-states at each FPA. In post-processing, co-located information in each detector is combined to reproduce the Stokes parameters (I, Q, U) of the original beam. Simultaneous polarization imaging by the three detectors, across four spectral channels, allows high polarization accuracy with no moving parts.

100 The core of AirHARP's polarization sensitivity is the custom Phillips prism, shown in Figure 2. While this prism is typically designed to split colors, the AirHARP prism splits the polarization content of the original signal into the three AirHARP detectors. The prism is made of three individual glass elements, A, B, and C, of equal index of refraction. The prism is a major component of an optical train that contains eight other sequential elements and a 114° wide field front lens. These lenses are optimized

105 for optical throughput into the prism and create an imaging sensor that is telecentric in the image space.

This feature is critical to our calibration and will be discussed in later sections. Most importantly, this refractive design allows wide-field of view measurements in a 3U CubeSat housing (10x10x30cm).

The modified Phillips prism alters each detector's light path in a specific way. The incident beam first enters the prism at the front face of Element A and meets the boundary between Elements A and C. A custom splitting coating at the boundary reflects 33% of this light back into Element A. Reflections like this reduce P-polarization and preserve S-polarization. Transmissions do the reverse. To boost the efficiency of the final polarization measurements, we align the Detector A polarizer with this S-polarization state, which is defined as 0°. The light path defined by the wide FOV front lens, optical train, the prism, the 0° polarizer, and the Detector A FPA is called *Sensor A*. The convention of our polarimetric calibration is relative to this Sensor. The two other light paths through the optics define Sensors B and C.

The light that passes through this boundary contains primarily P-polarized light. At the interface between Elements B and C, another thin-film coating splits the light intensity 50%-in-reflection and 50%-in-transmission. So far, the polarization content of this beam has changed by a transmission through the Element A-C interface and a reflection at the B-C interface. Therefore, the light incident on Detector C is a weak mixture of S- and P-states. The detector polarizer can be set at any angle with minimal effect on polarization efficiency. During optimization testing, we found the best orientation to be 90° for the Detector C polarizer, and likewise 45° for the Detector B polarizer. This 45° relative separation between the polarizers is optimal to discriminate measured states of polarization in our design (Tyo et al. 2006). Sensors B and C each account for 33% of the intensity of the incident beam, as well. Therefore, the AirHARP optics splits the incident light intensity equally among the three Sensors, each Sensor images a spatially identical scene, and each Sensor is sensitive to a different angle of polarized light.

Light that passes through the prism and detector polarizer is categorized by a custom interferometric filter on the detector surface. Each detector pixel maps to a specific spectral band, defined by one of the 120 view sectors. AirHARP produces a pushbroom of a ground scene in a single view sector by flying over the scene and acquiring images one after the other. The co-located information from multiple view sectors can provide high angular coverage on the cloudbow at 670nm (McBride et al. 2020) and multi-angle sampling of aerosol optical, shape, size, and loading properties (Hasekamp and Landgraf 2007, Wu et al. 2015, Puthukuddy et al. 2020) and atmospheric correction (Frouin et al. 2019). Aerosol

and cloud properties retrieved by AirHARP (and future HARP instrument) measurements may complement our existing climate record and advance our understanding of climate change uncertainties, feedbacks, and forcings (Boucher et al. 2013).

The AirHARP instrument and spaceborne version, the HARP CubeSat, were funded by the NASA Engineering Science and Technology Office InVEST program as a demonstration of advanced, miniaturized Earth science technology for future satellite missions. The HARP CubeSat recently completed a two-year mission in the 425km apogee orbit of the International Space Station. AirHARP was built specifically for science aircraft, like the NASA B-200 and ER-2, and demonstrated the HARP design and capabilities in field campaigns before and during the CubeSat mission. AirHARP flew successfully in two NASA aircraft studies in 2017: the Lake Michigan Ozone Study (LMOS) in the summer (McBride et al. 2020) and Aerosol Characterization from Polarimeter and Lidar (ACEPOL) in the fall (Knobelspiesse et al. 2020). A third, highly advanced version of the HARP concept, HARP2, recently launched on-board the NASA PACE mission (McBride et al. 2019). HARP2 achieves global coverage in two days and, as of this writing, has taken over 2 months of global radiance and polarization imagery. HARP2 anticipates a nominal mission lifetime of three years.

While the calibration discussed in later sections is the general scheme for any of the HARP instruments, plots, tables and figures correspond the AirHARP instrument, unless otherwise noted. Whenever the term HARP is used without an "Air" prefix or "CubeSat" suffix, it is in reference to a general HARP design.

## 3 Calibration Scheme for HARP Instruments

### 3.1 Detector Specifications and Background Correction

The calibration process of the AirHARP begins at the detector level. The AirHARP detectors are monochrome CCDs with a four-megapixel active focal plane array (FPA, Semiconductor Components Industries 2015). Relevant properties, such as quantum efficiency, read noise, and dark current, are given in Table 1. The typical image taken by the AirHARP detectors are shown in Figure 3a. The detector stripe filter creates the cross-track striping in the images seen below. The far left and right detector pixels are

masked, which defines the active science area of the FPA. The pixel values in these areas are compatible with a *dark image*, which is a snapshot taken when the entire FOV is blocked from illumination, shown in Figure 3b.

The first step in the AirHARP calibration begins at the detector level. Detectors generate a stable electrical bias across the FPA when they operate, which must be removed before science analysis. To account for this, we block all illumination from reaching the front lens (i.e. with a lens cap or internal shutter) and take 10 or more sequential images in each detector. These images are averaged together into a *dark template*. Creating this template image is called the *standard process* in this work going forward. The typical distribution of the dark template is given in Figure 3b. The region of lower pixels on the left-hand side of the image is typical of CCDs and occurs as photoelectrons move toward the serial register. A typical dark signal for the AirHARP detectors is 40 counts when operating at room temperature. In general, the background correction is as follows:

$$DN_{BC} = DN_{raw} - DN_{dark}, \tag{1}$$

where *DN_{BC}* is the background corrected image *digital numbers* or counts, *DN_{raw}* are the raw image counts, and $DN_{dark}$ represents the dark template counts. Whenever the term *raw* is used it refers to any HARP image, whereas subscripts other than *raw* describe an image captured in a different environment. Furthermore, counts may be called *analog-digital units* (ADU) in this work, if relevant.

All HARP iterations have an internal shutter, which is actuated for in-flight dark captures. This shutter does not contribute to polarization imaging and defaults to an open configuration outside of the optical path as a fail-safe. If we cannot take dark captures on-orbit or during field campaigns for any reason, we can create a *synthetic dark* by scaling a normalized dark template from the lab by an average of all along-track counts in the vignetted areas of a live data capture (typically over cross-track pixel indices 0-100, seen in Figure 3b):

$$DN_{dark} = \widehat{DN}_{dark}\overline{DN}_{raw}^{*} \tag{2}$$

where *DN_{dark}* is the estimated dark image counts and $\widehat{DN}_{dark}$ is a normalized dark template image from the lab. $\overline{DN}_{raw}^{*}$ represents a spatial mean of pixels in the vignetted area of a raw image capture (similar to Figure 3a). Eq. (2) creates a full-field dark image for each sensor that is used in the following calibration steps and in the Level 1B processing of AirHARP flight imagery. If Eq. (2) is required, i.e. the $DN_{dark}$

here is substituted into Eq. (1). This technique is currently used to correct AirHARP L1B datasets in Version 002 and accounts for the possibility of internal shutter failure on-orbit.

190    In the following sections, we limit our discussion to the 670nm channel, unless otherwise noted. Similar performance for the other three channels can be found in official ancillary basis documents (ACEPOL Science Team, 2017).

## 3.2 Non-Linear Correction

AirHARP sensors are commercial CCDs. They are subject to non-linearity in their analog-to-
195    digital conversion (ADC). For very bright targets, like sunglint, the Earth's limb, or direct solar exposure, pixels may saturate at the top of the detector well (44,000 electrons or $2^{14}$ counts). Saturated pixels cannot convert any extra photoelectrons to counts, but CCDs are known to have a non-linear gain near saturation and potentially at very low light levels.

The detectors must have a well-characterized for accurate science retrievals, too. We characterize
200    non-linearity by taking images of a stable source at a single illumination level. Each image is taken at a longer integration time than the last, and the testing ends when all sensors and channels are saturated. To perform this test, the AirHARP instrument was placed ~1m from the entrance aperture of the NASA GSFC "Grande" sphere. The AirHARP detector integration times are set near 4 ms to start. The integration times of each sensor are increased, and images are taken until all three sensors and channels
205    saturate. The stability of the source is tracked over the testing window using a current monitor. The standard process is used to form a template image at each integration time and for each detector. We take a small pixel bin (~4x4) along the optical axis in the templates and plot those values against their integration times. This process is performed for each channel and sensor. An example for the 670nm channel is shown in Figure 4a, for the three AirHARP detectors (Sensor A in cyan, Sensor B in magenta,
210    Sensor C in black). There is a monotonic, positive relationship between integration time and detector

counts, up until the saturation point, $2^{14}$ ADU. We identify a set of data points with minimal deviation from a linear response (<3000 ADU), and compare the linear fit over those points to the rest of the data:

$$DN_{corr} = DN_{linfit} - DN_{BC} = n_0 \, DN_{BC}^2 + n_1 DN_{BC} + n_2, \tag{3}$$

215

where $DN_{corr}$ is the non-linear corrected counts, $DN_{linfit}$ is the fit performed on the linear region, $DN_{BC}$ is the counts data derived from Eq. (1), and fit parameters $n_0$, $n_1$, and $n_2$ are free parameters. In our Figure 4b example, the residual ($DN_{linfit} - DN_{BC}$) is the y-axis and the x-axis is $DN_{BC}$. The maximum non-linear deviation at 670 nm is ~5% in Sensor A, found by taking the ratio $DN_{linfit}/DN_{BC}$. This ratio agrees with the 6% non-linearity limit in KAI-04070 detector spec, and similar agreement is found for other channels and sensors. Background correction and non-linearity occur before any other step in the Level 1B processing pipeline for HARP data. We perform non-linearity early in the calibration pipeline to check detector-level anomalies. Because the radiometric information in the scene data comes from all three detectors, it is not feasible to characterize linearity during radiometric calibration, like MODIS (Aldoretta et al. 2019). Non-linear correction early in the calibration pipeline allows for a verification of the reciprocal test during absolute radiometric calibration (counts measured at a single integration time across a variety of lamp levels).

### 3.3 Flatfielding

Next, we characterize the pixel-to-pixel relative response of each detector. Any system with sequential optical elements will vignette photons toward the edge the FPA. Individual pixels may have a relative differential gain, as well. Both effects must be corrected. To account for this, images are taken of a homogenous target in a process is called *flatfielding*. Integrating spheres are typical sources. They create uniform illumination over their aperture and can depolarize the output to a level below 0.5% in visible wavelengths (McClain et al. 1994). Therefore, any heterogeneity in the images is due to the instrument, not the source. We use the "Grande" 101.6cm integrating sphere at NASA GSFC for major calibration activities and a portable LED hemisphere at UMBC during field campaigns or between GSFC

calibrations. To form the flatfield template, the full-FOV of the AirHARP instrument images the aperture of an illuminated integrating sphere, at an integration time where all channels are below saturation. The
240 images are full-size, full-resolution and resemble Figure 5a. A template image, created using the standard process, is corrected for background and non-linearity. This template is then interpolated by a smoothing algorithm, row-by-row. This step captures the structure of vignetting and other potential artifacts, such as optical etaloning and defects on the detector surface.

Figure 5b shows a cross-track line-cut for several 670nm view sectors: +27° (red), +14° (blue),
245 nadir (grey), -8° (green), and -20° (magenta) are shown. The x-axis is cross-track pixel index. The edge vignetted detector regions are neglected in the flatfielding process. The y-axis is detector counts (ADU). Each curve is artificially offset by +/- 500 or 1000 ADU for clarity, though the nadir curve corresponds directly to the y-axis values. The counts data for each row is smoothed using a 15-pixel sliding window average (black). The smoothing process also captures other stable artifacts in the images (i.e. oscillations
250 due to optical etaloning), that can be removed as part of this correction. We repeat this smoothing process for each channel and detector row until we arrive at a smoothed full-field template image, at the same size and resolution as the original data. We then normalize the smoothed signal of each channel by relevant pixels along the optical axis. This normalized, smoothed signal becomes the flatfield correction, $f$, for this channel and detector. Normalization is done so that the flatfield is scalable to any radiance level
255 in a field measurement. Each pixel in the FOV has a different value of $f$. The optical axis is chosen specifically as the location of $f=1$ to simplify the later steps in the calibration process that also use optical axis pixels. We then apply the flatfield correction at the pixel-level:

$$DN^* = \frac{DN_{corr}}{f(x,y)},\qquad(4)$$

260

where f is the value of the flatfield correction for that pixel, which is a function of cross-track and along-track pixel indices x and y, and the numerator of Eq. (4) is the same as Eq. (3). To verify the flat correction, we apply the flatfield to its generating dataset via Eq. (4). Figure 5c shows a histogram of the residuals after flatfielding all pixels in the same subset of view sectors as Figure 5b. The data point colors in Figure

265  5c map to the same view sector colors in Fig. 5b. The original signal is corrected down to signal-to-noise
(SNR) variations at the 0.005 level for each view sector. Figure 5c shows that this method is robust across
the FOV and accurately removes all systematic artifacts in the data. Moreover, this correction creates a
detector-specific flatfield $f$ for each of the four AirHARP channels.

The flatfield serves another critical role in the AirHARP calibration. AirHARP optics are
270  telecentric in the image space, and so all incident rays on the detector arrive at 0° angle-of-incidence
(AOI). This design prevents AOI-related artifacts in the images or dependency in the calibration
coefficients. Our flatfield represents the entire internal optical behavior of the system and simplifies our
next calibration steps in the process. We can derive channel-dependent coefficients at any location in the
FPA and spread that result to the rest of the FOV using the detector flatfields. This *telecentric technique*
275  is the method used in the following steps of our calibration process. We also verify these coefficients
using lab techniques and across the full FOV using field data in Sections 3 and 4.

## 3.4 Relative polarimetric calibration

### 3.4.1 Theoretical description

After the images are corrected for background, non-linearity, flatfield, and the detectors are
280  mechanically co-aligned in the image space, the instrument is ready for quantitative polarization

calibration. The theory of our calibration is given in Fernandez-Borda et al. (2009), though a brief treatment of the scheme is discussed here.

The polarization state of a light beam is described by the Stokes column vector, which is a time-average (designated by the enclosing brackets) of the real and imaginary components of the electric fields (Jackson 1962):

$$S = \begin{bmatrix} I \\ Q \\ U \\ V \end{bmatrix} = \begin{bmatrix} \langle E_\parallel E_\parallel^* + E_\perp E_\perp^* \rangle \\ \langle E_\parallel E_\parallel^* - E_\perp E_\perp^* \rangle \\ \langle E_\parallel E_\perp^* + E_\perp E_\parallel^* \rangle \\ i\langle E_\parallel E_\perp^* - E_\perp E_\parallel^* \rangle \end{bmatrix}, \tag{5}$$

where $E_\parallel$ and $E_\perp$ the parallel (S) and perpendicular (P) real components of the electric field (with their imaginary counterparts designated by *). The Stokes parameters represent total, linearly polarized, and circularly polarized radiance, which all carry units of W m$^{-2}$ nm$^{-1}$ sr$^{-1}$. The total radiance ($I$) is the sum of the parallel and perpendicular intensities of the beam. The linearly polarized radiances represent excesses of 0° over 90° polarization angles ($Q$), and 45° over 135° polarization angles ($U$), and the circularly polarized radiance represents the excess of left-circular over right-circular polarization ($V$). These four parameters fully describe the polarization state of a light beam and are related with two equations:

$$I^2 \geq Q^2 + U^2 + V^2, \tag{6}$$

and

$$DOP = \frac{\sqrt{Q^2 + U^2 + V^2}}{I}, \tag{7}$$

where $DOP$ is the degree of polarization, a dimensionless ratio between 0 and 1 that represents the amount of polarized light in the total intensity measurement. Note that in the absence of V, Eq. (7) becomes the

*degree of linear polarization* (*DOLP*). We will neglect the V parameter in this study, as it is negligible at
305   the top of the atmosphere (Hansen and Travis 1974) and not measured by AirHARP.

Ray traces through optical media, like lenses and prisms, are sequential and can be described by
linear algebra. A polarized beam traveling through an optical interface is related to the output beam by a
Mueller matrix:

$$\begin{bmatrix} I \\ Q \\ U \end{bmatrix}_{sca} = \begin{bmatrix} M_{11} & M_{12} & M_{13} \\ M_{21} & M_{22} & M_{23} \\ M_{31} & M_{32} & M_{33} \end{bmatrix} \begin{bmatrix} I \\ Q \\ U \end{bmatrix}_{inc} , \tag{8}$$

where subscripts *inc* and *sca* represent the Stokes vector for the incident beam and scattered beam,
respectively. The $M_{ij}$ elements describe how the medium changes the nature this beam. The M-matrix in
Eq. (8) may be a single optical element, or an optical train. This matrix is a product of several matrices
315   that describe the sequential optical elements of the AirHARP system:

$$\begin{bmatrix} I \\ Q \\ U \end{bmatrix}_{det} = M_{polarizer}\, M_{prism}\, M_{train} \begin{bmatrix} I \\ Q \\ U \end{bmatrix}_{inc} = \boldsymbol{M_{system}} \begin{bmatrix} I \\ Q \\ U \end{bmatrix}_{inc} , \tag{9}$$

where the subscript *det* now corresponds to the Stokes vector incident on the detector FPA, and the
320   subscripts *polarizer, prism,* and *train* correspond to the Mueller matrices of the detector polarizer, the
optical path through the Phillips prism, and the optical lens train in the housing. In theory, each of these
M-matrices defined in Eq. (9) contain internal Mueller matrices for coating interfaces, lenses, and prism
elements, but these are difficult to characterize individually from a single full-system detector
measurement. Therefore, these are combined into one global M-matrix ($M_{system}$) that characterizes the
325   entire optical train.

The HARP detectors only register intensity values, meaning it is not possible to measure the $Q_{det}$
and $U_{det}$ information directly in Eq. (9). However, because the linear polarizer in front of each detector is
oriented at a different angle, the intensity measured at the FPA encodes information about that

polarization state. We can retrieve the original polarization state of the Earth scene by combining intensity information from the three detectors (Fernandez-Borda et al. 2009). We can isolate the matrix components from the Eq. (9) matrix that contribute to $I_{det}$, for each detector, and form a relationship between detector counts and the incident Stokes state:

$$\begin{bmatrix} DN^*_{\det A} \\ DN^*_{\det B} \\ DN^*_{\det C} \end{bmatrix} = \begin{bmatrix} M_{11,det\ A} & M_{12,det\ A} & M_{13,det\ A} \\ M_{11,det\ B} & M_{12,det\ B} & M_{13,det\ B} \\ M_{11,det\ C} & M_{12,det\ C} & M_{13,det\ C} \end{bmatrix} \begin{bmatrix} I \\ Q \\ U \end{bmatrix}_{inc} = \boldsymbol{M}^* \begin{bmatrix} I \\ Q \\ U \end{bmatrix}_{inc}, \qquad (10)$$

where the $M_{1j,\ det\ X}$ coefficients represent the first row of the Mueller matrix for the light path through the optical system into that specific detector (j = 1, 2 or 3) and $DN^*_{\det X}$, represents the corrected detector counts from Eq. (4), where X could be A, B, or C. This matrix with $M_{1X}$ coefficients is $\boldsymbol{M}^*$. Note that $\boldsymbol{M}^*$ is not a Mueller matrix.

## 3.4.2 Application in the laboratory

The purpose of the polarimetric calibration of the AirHARP instrument is to derive $\boldsymbol{M}^*$ and/or its inverse using Eq. (10). To do this, we use an integrating sphere as our source and a 1-inch Moxtek wire-grid linear polarizer, placed at the aperture of this sphere to modify the polarization content of the beam. The Moxtek is a high efficiency, high contrast polarizer suitable for the 400-900nm wavelength range. We set this polarizer in a Thorlabs rotational mount and accurately control the angle of polarization entering the AirHARP instrument to 0.001°. The Moxtek is highly reflective, so we also tilt the polarizer along the AirHARP optical axis by 10° to avoid back-reflections into the AirHARP optics (van Harten et al. 2018). The polarizer is characterized before any testing and its starting orientation is verified by an external reference polarizer.

The optical axis of the HARP instrument is placed along the axis between the center of the Moxtek polarizer and the aperture of the integrating sphere such that the HARP image is illuminated at nadir. The integrating sphere is set to a lamp level below the saturation limit of all HARP channels. The Moxtek is mechanically rotated at intervals of 10°. Simultaneous images are taken at each detector and Moxtek

angle. Because we defined the starting orientation of the Moxtek, the relative Stokes state at each angle
is well-known, with $Q/I = cos\ 2\vartheta$ and $U/I = sin\ 2\vartheta$ (Kliger et al. 1990), where $\vartheta$ is the rotation angle. The absolute radiometry is not important at this stage, however, the relative stability of the output over the testing window is monitored.

The optical path from the HARP front lens to a single FPA creates a single partial polarizer (i.e. Eq. 9). Therefore, this test creates a two-polarizer system. Malus' law explains the observed counts at each detector as a function of $\vartheta$. To account for optical complexity of HARP, we use a general fit:

$$DN^*_{det\,X}(\vartheta) = \alpha\ cos^2[\vartheta - (\vartheta_X - \beta)] + \gamma, \tag{11}$$

where the shorter subscript *det X* represents the background, linearity, and flatfield-corrected counts in a single detector (i.e. X could be A, B, or C) during this test and $\alpha, \beta$, and $\gamma$ are fit parameters. $\vartheta_X$ is the nominal polarizer angle for a detector X, determined during AirHARP pre-assembly testing. Figure 6 shows examples of Malus curves and fits to Eq. (11) for the three detectors and four channels, using co-located Moxtek data along the AirHARP optical axis.

The amplitude of the curves is related to the $\alpha$ and $\gamma$ parameters, the phase to $\beta$, and the extinction ("lift" off the zero line) to $\gamma$. Any global bias due to the Moxtek polarizer itself is negligible or removable for reasons stated above. Surface inhomogeneities on the polarizer may impart higher-order frequencies in the signal, which can be accounted for by Fourier decomposition (Cairns et al. 1999). A separate sensitivity study using a reference polarimeter and a rotating polarizer in our lab suggests that Fourier modes at the 0.005 level (such as $sin4\vartheta$) stem from surface variations and are removed during this analysis. After normalizing each Malus curve by the maximum of the curve in *det A* for each channel and

detector, and inverting the matrix in Eq. (10), we come to a final relationship that completely represents this step:

$$
\begin{bmatrix} 1 \\ -\cos 2\vartheta \\ \sin 2\vartheta \end{bmatrix}_{inc} = \begin{bmatrix} C_{11,} & C_{12} & C_{13} \\ C_{21} & C_{22} & C_{23} \\ C_{31} & C_{32} & C_{33} \end{bmatrix} \begin{bmatrix} DN^*_{\det A}(\vartheta) \\ DN^*_{\det B}(\vartheta) \\ DN^*_{\det C}(\vartheta) \end{bmatrix} (max(DN^*_{\det A}(\vartheta))^{-1}, \tag{12}
$$

380

where the Stokes parameters (I, Q, U) are replaced with their theoretical forms and the matrix $\mathbf{C} = (\mathbf{M}^*)^{-1}$ from Eq. (10). This $\mathbf{C}$ is defined in Fernandez-Borda et al. (2009) as the *characteristic matrix*. The $\mathbf{C}$ translates normalized, corrected detector counts to normalized Stokes parameters for pixels along the optical axis (though applicable to polarization measurements anywhere in the FOV). The $\mathbf{C^{-1}}$ has an 385 analytic form based on the angle of the polarizers used for the three detectors (Schott 2009):

$$
C^{-1} = \begin{bmatrix} f_A & f_A\, g_A \cos 2(\theta_A - \beta_A) & f_A\, g_A \sin 2(\theta_A - \beta_A) \\ f_B & f_B\, g_B \cos 2(\theta_B - \beta_B) & f_B\, g_B \sin 2(\theta_B - \beta_B) \\ f_C & f_C\, g_C \cos 2(\theta_C - \beta_C) & f_C\, g_C \sin 2(\theta_C - \beta_C) \end{bmatrix}, \tag{13}
$$

Coefficients define the transmission of the light through the entire optical system ($f_X$), polarizing 390 efficiency ($g_X$), and phase offset ($\beta_X$) relative to the nominal detector polarizer angles ($\theta_X$) from Eq. (11). This characteristic matrix can be solved in two ways: a least-squares approach on Eq. (12) using data from at least three Moxtek polarizer angles, or a similar least-squares approach on the inverse matrix, Eq. (13). We prefer the former in this study, but consistency checks with the latter are useful. Table 2a gives the characteristic matrix coefficients with relative uncertainties using the least-squares method and Table 395 2b gives example values with uncertainties using the parametric method. Both tables shown below represent a 4x4 nadir pixel bin for the 670nm channel for AirHARP.

Table 2b shows that the nominal AirHARP polarizer angles ($\theta_X$) can deviate from their expected values ($\beta_X$). Note that $\theta_X - \beta_X$ is the perceived polarization orientation of the entire light path from the perspective of each FPA. Retardances induced by the prism and/or detector polarizer will contribute to 400 $\beta_X$. Note that the coefficients are significantly different from the Pickering matrix, the ideal C-matrix for

a AirHARP-like system (Schott 2009). The characteristic matrix coefficients shown in Table 2a use the polarizer datasets alone, though current AirHARP L1B processing through Version 002 includes input from low DOLP sources (integrating spheres, partial polarization generators) for closure on the entire DOLP range. The errors and values in Table 2a can be used to calculate the propagated uncertainty in the relative Stokes parameters, which is derived from Eq. (12):

$$\sigma_{S_i}{}^2 = (max(DN^*_{\det A}(\vartheta))^{-2} \sum_{j=1}^{3} \left[ \left( DN^*_{\det j} \, \sigma_{C_{ij}} \right)^2 + \left( C_{ij} \, \sigma_{DN^*_{\det j}} \right)^2 \right], \tag{14}$$

where $\sigma_{S_i}$ is the standard deviation of the Stokes parameters (denoted generally by subscript $S$). We use the $i$ iterant to define the Stokes parameter: [1,2,3] corresponds to [I,Q,U], and can be used interchangably. $DN^*_{\det j}$ is the result from Eq. (11) where the $j$ iterant [1,2,3] corresponds to sensors [A, B, C]. $\sigma_{C_{ij}}$ is the uncertainty quoted in Table 2a for the $C_{ij}$ matrix element, and $\sigma_{DN^*_{\det j}}$ is the propagated uncertainty of the detector counts measurement. The value for $\sigma_{DN^*_{\det j}}$ involves random elements such as shot, read, and dark current noises, and systematic elements from background, flatfield, and non-linear correction. It may also include stray light and other noises that are difficult to decouple. At the integration times we use, shot noise and potentially scene spatial variability can dominate, so the standard deviation of data from a real AirHARP superpixel, a rectangular, connected set of along-track and cross-track pixels, is used.

## 3.5 Radiometric calibration

### 3.5.1 Relative spectral response

With the polarimetric calibration complete, the next step is radiometric calibration, which requires knowledge of spectral response. The AirHARP instrument uses several filters to define the four nominal wavelength channels, with bandwidths in parentheses: 440 (16), 550 (13), 670 (18), and 870 (39) nm. The

spectral response function (SRF) is defined by a multi-bandpass filter (MBPF) and the stripe filter on top of each detector.

425       To validate these filter specs, we placed the AirHARP instrument in the aperture of a separate 25.6cm integrating sphere at NASA GSFC, fed by an Ekspla laser source. The Ekspla is a scanning monochromator capable of 1 nm precision, over a 200-1000nm range. We set the Ekspla source at a given wavelength and verified each output channel and bandwidth using an external Avantes spectrometer. We use the spectrometer output to correct the AirHARP measurements for any variation in Ekspla laser power 430  over the course of the testing period.

      The standard process is used on AirHARP images that are taken at each Ekspla wavelength setting. The Ekspla channels were chosen using *a priori* knowledge of the filter spectra from the manufacturer. A higher density of images were acquired in-band than out-of-band to capture the structure of the in-band SRF. Figure 7a shows AirHARP images of the integrating sphere, illuminated by four in-band Ekspla 435  wavelengths. When the Ekspla is set to an in-band channel near 670nm, the 60 AirHARP red view sectors are illuminated. For the other AirHARP channels, the sparser distribution of 20 view sectors appear whenever the Ekpsla is in-band. For Ekpsla wavelengths rejected by the AirHARP system, the images are compatible with dark signal (Figure 3b).

      Using the telecentric technique, we take a small region of nadir pixels, correct their values via the 440  process leading up to Eq. (4), and plot them against Ekspla wavelength for a single HARP channel. Figure 7b shows the SRF for AirHARP Sensor 1 (blue dots), Sensor 2 (green dots), and Sensor 3 (orange dots) for 440nm (left), 550nm (left-center), 670nm (right-center), and 870nm (right). Because the SRF data is noisy, even after correction from an external spectrometer, we use a general super-Gaussian fit of order six (plotted in gray) to simplify the following analysis. Figure 7b also shows a differential SRF for the 445  AirHARP 440nm band, which is likely due to manufacturer error in the thin-film coating for the AirHARP prism interfaces or detector stripe filters. This 440nm SRF differential is unique to AirHARP; we see no evidence of this in the HARP CubeSat or HARP2 440nm designs (Sienkiewicz et al. 2024, *in prep*). We

are pursuing several corrections for the AirHARP 440 nm spectral differential at the detector level and L1B stage, though further details are beyond the scope of this work.

450        This testing benefits two studies: (1) calculation of extraterrestrial solar irradiance, used to convert radiance measured at the top-of-atmosphere (TOA) to reflectance (or reflectance factor), and (2) radiometric calibration. To perform (1), we integrate the solar spectrum (here, using the American Society for Testing and Materials Standard Extraterrestrial Spectrum Reference E-490 Air Mass Zero (AMZ) database (NREL 2000) inside the SRF for each HARP wavelength:

$$F_0(\lambda) = \frac{1}{\Delta\lambda} \int_{\lambda_i}^{\lambda_f} B(\lambda)\, SRF(\lambda)\, d\lambda, \tag{15}$$

455

where $\lambda$ is the wavelength (subscripts $i$ and $f$ denoting the shorter- and longer-wavelength edges of the spectral band) in nm, $\Delta\lambda$ is the bandwidth in nm, $B(\lambda)$ is the solar spectral irradiance in W m$^{-2}$ nm$^{-1}$ and SRF($\lambda$) is the spectral response function. We only use the structure of the in-band channel in Eq. (15),

460  and fit each window to a sixth order super-Gaussian function, due to unexplained noise in the dataset larger than the uncertainty of each data point (especially at 870nm). Normalized out-of-band rejection is at or below 0.001 for the 300 to 1050 nm range, as well. Analysis of the second-order in-band differences relative to this theoretical fitting are ongoing but are not expected to contribute significantly to the L1B

data product (AirHARP 440nm notwithstanding). Table 3 shows the details of our spectral response
465  testing and the extraterrestrial solar irradiance, $F_0$, calculated using Eq. (16), for each channel.

The final column of this chart is used to convert measured radiances to reflectance factor as per:

$$\rho(\lambda) \ = \ \frac{\pi\, L(\lambda)}{F_0(\lambda)}, \tag{16}$$

where $\rho(\lambda)$ is the reflectance factor and $L(\lambda)$ is radiance in units of W m$^{-2}$ nm$^{-1}$ sr$^{-1}$, assuming a
470  Lambertian scattering distribution of light in the pixel. We can divide Eq. (16) by the cosine of the solar
zenith angle convert to TOA reflectance.

### 3.5.2 Gain characterization

Our radiometric calibration translates the normalized Stokes parameters to calibrated radiances
(W m$^{-2}$ nm$^{-1}$ sr$^{-1}$). This step gives scientific weight to our measurements and allows us to retrieve radiative
475  properties about the atmosphere and surface. Again, integrating spheres are optimal for this testing. For
example, the radiometrically calibrated NASA GSFC "Grande" sphere is traceable to the National
Institute of Standards and Technology (NIST) with calibration uncertainties publicly available for a
comparable sphere (Cooper and Butler 2020). The spectral sensitivity of "Grande" peaks around 1 $\mu$m,
and each of the nine lamps add linearly to the total illumination.
480  We set the AirHARP instrument in the same conditions as the polarimetric calibration, discussed
in 1.4, except with no polarizing element between the instrument and integrating sphere. Because the
lamps are incandescent sources, we adjust the AirHARP detector integration times to capture enough
signal in the blue channel and stay out of saturation in the NIR. The standard process is used at each lamp
level to create template images. Using the telecentric technique, we select a small nadir pixel bin for a
485  given wavelength, correct the values using the process leading up to Eq. (4), and apply the characteristic
matrix for that channel to the co-located data in each detector. The sphere output is depolarized, so the
resulting Stokes parameters Q and U are statistically zero and the total intensity, I, contains all the
information content. As per Eq. (12), the resulting I is in counts, yet represents the band-weighted signal
measured by a particular AirHARP channel. To find the equivalent radiance levels as observed by

AirHARP, the solar spectrum, $B(\lambda)$, is replaced by the Grande SRF in Eq. (15) (Cooper and Butler 2020) and this calculation is performed for each lamp and wavelength. The radiometric calibration derives the slope (W m$^{-2}$ nm$^{-1}$ sr$^{-1}$ ADU$^{-1}$) that translates the normalized AirHARP intensities to the calibrated radiances:

$$L_{lamp} = k \left( C_{11} DN^*_{\det A} + C_{12} DN^*_{\det B} + C_{13} DN^*_{\det C} \right) + \epsilon, \tag{17}$$

where $L_{lamp}$ is the calibrated radiances (W m$^{-2}$ nm$^{-1}$ sr$^{-1}$) at that lamp level. The parameter $k$ is our gain factor, and $\epsilon$ is a linear bias. For all channels, the linear bias $\epsilon$ is compatible with zero within three

standard deviations of the least-squares fit error on this coefficient. Therefore, the general calibration equation for the AirHARP instrument is the following:

$$
\begin{bmatrix} I \\ Q \\ U \end{bmatrix} = k \begin{bmatrix} C_{11} & C_{12} & C_{13} \\ C_{21} & C_{22} & C_{23} \\ C_{31} & C_{32} & C_{33} \end{bmatrix} \begin{bmatrix} DN^*_{\det A} \\ DN^*_{\det B} \\ DN^*_{\det C} \end{bmatrix},
$$

(18)

and the complete, propagated uncertainty of the L1B calibrated radiances:

$$
\sigma_{S_i}{}^2 = \sum_{j=1}^{3} k^2 \left[ \left( DN^*_{\det j} \, \sigma_{C_{ij}} \right)^2 + \left( C_{ij} \, \sigma_{DN^*_{\det j}} \right)^2 \right] + \left( C_{ij} \, DN^*_{\det j} \, \sigma_k \right)^2,
$$

(19)

where the subscripts follow the same convention as Eq. (14).

## 4 Validation of calibrated measurements

### 4.1 Nadir coefficients

Before we evaluate the calibration over the entire FOV, it is important we validate the same lens locations that we used to calibrate the instrument. Here, we evaluate the nadir coefficients for a range of partially polarized DOLP signals, like those AirHARP observes in field data.

In the atmosphere, DOLP measurements close to 1 occur only at certain geometries with sunglint over dark ocean or Rayleigh scattering in the ultraviolet. More often, a complex atmosphere-land-ocean scene generates partially polarized light ($0 < $ DOLP $ < 1$). To simulate this, a partial polarization generator box (POLBOX), a Fresnel device comprised of two rotatable glass blades at equal index of refraction, is used (Figure 8a). This polarization state generator is widely used for lab validation of spaceborne polarimeters (van Harten et al. 2018, Li et al. 2018, Smit et al. 2019). Any deviation in the DOLP retrieval gives the lab calibration uncertainty of the HARP system, after systematic POLBOX uncertainty is

accounted for. The POLBOX DOLP is analytic and the values at each blade setting can be determined by the sequential Fresnel interactions at each air-glass interface:

$$DoLP_{POLBOX} = \frac{\alpha(n,\lambda)\cos^2(2\theta) + \beta(n,\lambda)\cos(2\theta) + \gamma(n,\lambda)}{\varepsilon(n,\lambda)\cos^2(2\theta) + \mu(n,\lambda)\cos(2\theta) + \omega(n,\lambda)} \quad (20)$$

525

where $\alpha, \beta, \gamma, \varepsilon, \mu,$ and $\omega$ are glass-specific coefficients, dependent on refractive index, $n$, and wavelength, $\lambda$, and $\theta$ is the glass blade angle. For our test, we keep the POLBOX glass blades perpendicular to the table, and take HARP images at increasing blade angles. The angle of the blades is controlled by a fine micrometer dial, and the angle is known within 0.25°. The data is corrected through

530 the process leading up to Eq. (4), and the pre-computed calibration matrices are applied for each wavelength and image in the dataset. As mentioned above, the characteristic matrix used in this validation includes Moxtek polarizer data and input Stokes vectors that represent unpolarized light for closure over the entire DOLP range. Using the same nadir pixel bin that was used for calibration, the measured Stokes parameters at each POLBOX blade angle are processed into the DOLP via Eq. (7) (neglecting V) and

535 these results are compared to Eq. (20) for each blade angle and wavelength.

The measured DOLP from the HARP system is within ±0.5% (with one sigma uncertainty of 0.25% in DOLP) of the true POLBOX values for all wavelengths, given a 4x4 pixel nadir bin, as shown in Figure 8b-c. Glass blade angles (<5˚) that create back reflections in the wide HARP FOV are neglected from the comparison. Removing these angles has a negligble impact on the comparison, as the theoretical

540 DOLP at 10˚ is still quite low (~4%) and still represents a depolarized environment. The POLBOX itself imparts a static DOLP uncertainty of 0.0015, related to the uncertainty in the glass blade angle (Li et al. 2018). This experiment is only limited by the intensity of the integrating sphere, which here was no less than 0.09 in reflectance (440nm). This level is a bit higher than the typical aerosol signal used in theoretical experiments ($L_{typ}$), but it is challenging to balance integration time and saturation in a single

545 lab measurement when all channels are simultaneously exposed. Even so, we conclude that the HARP design allows for a highly accurate pre-launch DOLP baseline for all channels, relative to recommended

cloud and aerosol science uncertainty benchmarks (NASA 2015, NASA 2021). A limited error model is given in the Appendix, and a comprehensive version is anticipated in future work.

## 4.2 Full FOV intercomparisons with field data

### 4.2.1 AirHARP participation in the Aerosol Characterization with Polarimeter and LIDAR (ACEPOL) campaign

Sensitivity tests in the lab allow us to characterize the HARP instrument in a well-controlled setting. However, these environments can be limited by resources and time, and this can impact how much of the FOV, spectral channels, and dynamic range are characterized. To validate the full FOV calibration, we take field data and compare how the HARP instrument measures the multi-angle reflectance factor and polarized signal with a similar MAP over a common target.

AirHARP participated in two NASA aircraft campaigns in 2017: the Lake Michigan Ozone Study (LMOS, Stanier et al. 2017) and Aerosol Characterization from Polarimeter and Lidar (ACEPOL, Knobelspiesse et al. 2020). LMOS took place over Lake Michigan and eastern Wisconsin from May 25 to June 19 2017 and ACEPOL over the southwestern United States and eastern Pacific Ocean from October 23 to November 9 2017. LMOS was AirHARP's debut and was the only instrument of its kind taking measurements during this period. ACEPOL, on the other hand, included two lidar and four polarimeter instruments on the aircraft, including AirHARP. A major goal of the ACEPOL campaign was to compare different polarimeter concepts over common targets, improve cross-calibration studies, and develop new synergistic algorithms for retrieving aerosol, cloud, land, and ocean properties.

During ACEPOL, these six instruments observed over 30 scenes including urban cities, coastal oceans, dry lakes, cloud decks, and prescribed wildfire smoke. Two of these targets are best suited for reflective solar band calibration and validation: sunglint over dark ocean and the Rosamond Dry Lake, a flat desert site in California. Sunglint is highly polarized at some geometries, reaching DOLP of nearly 1 in the optical regime. Off-glint, polarization is reduced and low ocean albedo is useful to validate dim reflectances. The sunglint signal can be modeled accurately, if the viewing and solar geometry are known and aerosol and Rayleigh scattering are removed. The appearance of sunglint depends on the ocean

surface wind speed, which can roughen the surface and break up the signal (Cox and Munk 1954). Even despite strong surface winds, the ocean surface is considered flat from a viewing altitude of 20km and requires no special topography correction to the data. Multi-angle polarimeters, like AirHARP, measure the way the sunglint signal varies with viewing angle, and can reproduce a discrete intensity and polarization profile with angle. Therefore, sunglint datasets are very convenient to use for calibration validation. The Rosamond Dry Lake is also a useful calibration target: it is a pseudo-invariant, highly reflective surface with a low DOLP profile. We use several ACEPOL ocean and desert datasets as a limited demonstration that our telecentric technique captures the expected performance of the AirHARP instrument across the FOV.

Because the focus of this work is calibration and not data intercomparisons, we will present the following study in a simple and limited sense. The Research Scanning Polarimeter (RSP) instrument was chosen as our validator because it best matches the along-track angular sampling of HARP, shared the same wing of the ER-2 with AirHARP during ACEPOL, and has the longest history of accurate, validated polarimetric measurements. The following describes the process used to co-locate AirHARP and RSP measurements at similar viewing angles:

1. A target of interest and reference lat-lon pair is identified and the closest scan in the RSP data is found. The average lat-lon pair of this scan becomes the new reference lat-lon point.
2. The algorithm finds the closest matching view zenith (VZA) and view azimuth (VAA) angles between AirHARP and RSP over this common target. The search finds a successful match if VZA difference is <1° and VAA difference is <5° degrees.
3. The lat-lon coordinate of the matching RSP measurement is now the updated lat-lon point for comparison.
4. A spatial mask that accounts for the 220 m RSP footprint and smear profile (Knobelspiesse et al. 2018) is applied to the AirHARP pixels around this lat-lon point. The resulting spatially-weighted

mean and ed standard deviations for VZA, VAA, solar azimuth (SAA) and zenith (SZA), I, Q, U, and DOLP are logged for AirHARP and the matching respective values for RSP.

600   5.  This process is repeated for all relevant spectral channels.

The intercomparison is validated using an error-normalized difference in both reflectance and DOLP for the three shared channels individually. We use the error models for both AirHARP and RSP (see Appendix) to study how well their measurements agree within their mutual uncertainty. Similar work in

605   multi-angle polarimetric intercomparisons was done in Knobelspiesse et al. (2019). The following is our metric:

$$\chi = \frac{\rho_{AirHARP} - \rho_{RSP}}{\sqrt{\sigma^2_{\rho,AirHARP} + \sigma^2_{\rho,RSP}}}, \tag{21}$$

610   where $\rho$ is the reflectance measurement, and $\sigma_\rho$ is the one-sigma reflectance uncertainty. Eq. (21) will be used similarly for DOLP measurements. If the error models adequately describe the measurement, we expect the residuals normalized by their uncertainties to have a normal distribution. In other words, if 68.27% (95.45%) of the Eq. (21) results lie between $\pm 1$ ($\pm 2$), this suggests general agreement and that there are no systematic influences on the comparison. This also suggests that the AirHARP calibration

615   can sufficiently reproduce reflectance and DOLP of Earth scenes relative to a similar, co-located multi-angle polarimeter. The following will discuss the results of the AirHARP and RSP intercomparison over both ocean and desert sites during the ACEPOL campaign.

**4.2.2 Results and Discussion**

620

The full FOV comparison with RSP uses two ocean cases from October 23, 2020 and five desert cases from October 25, 2020, taken during the ACEPOL campaign. The ocean captures occurred 30 minutes apart off the coast of California: the first at 20:10 UTC over 35.12° N 124.75° W and the second at 20:49 UTC over 31.75° N 122.38° W. We will identify the earlier as Ocean 1 and the later as Ocean 2 going

625 forward, and both are parallel to and slightly off the solar principal plane. The five desert cases were taken on October 25, 2020 over the Rosamond Dry Lake site in California, also 30 minutes apart: 17:28, 17:55, 18:26, 18:55, and 19:28 UTC. These captures will be identified as Desert 1 through 5, respectively, and all targeted the general region around 34.83° N 118.07° W.

The AirHARP and RSP data were ordered for these dates, times, and locations, and the co-location

630 procedure described in Section 3.2.1 was followed for each of the sites and the three spectral channels in common to both instruments: 550, 670, and 865 or 870nm. We do not show a comparison with the AirHARP 440nm band because there is no comparable RSP channel and for SRF reasons mentioned above that could complicate the interpretation of the results. The AirHARP 550 (13), 670 (18), and 870 (39) nm and the RSP 550 (20), 670 (20), and 865 (20) nm spectral bands are generally compatible. We

635 also do not expect any significant differences in the signal of the desert or glint targets relative to SRF differences. We did not perform any spectral matching in this work.

Figure 9 shows a multi-angle comparison of AirHARP and RSP for four of the seven ACEPOL datasets. RSP data is in black and the AirHARP desert (red) and ocean (blue) for both reflectance factor (first column, calculated via Eq. 17) and DOLP (second column). Three compatible channels are shown:

640 550nm (top row), 670nm (middle row), and 870nm (bottom row). The error bar on the AirHARP points is the sub-pixel standard deviation of the superpixel at each angle. This figure was developed by searching for the closest match between AirHARP and RSP reflectance factor and DOLP measurements over a similar view geometry. After all matches were found, the RSP data was interpolated to the AirHARP scattering angles. We can use Figure 9 to explore the angular information content in both desert and ocean

645 scenes. For the ocean cases, the reflectance factor is lower than 0.1 in all channels, but the DOLP range is wide, 0 to ~0.8. The desert cases were chosen specifically to contrast with sunglint. The desert cases shown in Figure 9 represent the same target viewed from two different headings, too. The dependency on viewing geometry is clear in the separation of the desert reflectance factor curves in all channels. These cases provide a range of geometry for intercomparison and adequate contrast in reflectance factor and

650 DOLP to validate our calibration.

The following is a more rigorous intercomparison. Figure 10 shows the error-normalized differences from the direct angle-to-angle, filtered matchups in reflectance (10a, not reflectance factor)

and DOLP (10b) taken by AirHARP and RSP across the seven datasets. Colored points are the relevant channels (550nm in cyan, 670nm in magenta, and 870nm in black), and the markers denote the different datasets. Across the three channels and scenes, we see that for reflectance 72.0% of the 286 filtered data points lie within $\pm 1$ and 94.8% within $\pm 2$. For DOLP, those numbers are similar: 65% and 91.0%. The ideal is 68.27% and 95.45% for a normally-distributed error residuals. This suggests that the mutual uncertainty reasonably describes the variance between AirHARP and RSP, and that their measurements are generally compatible. There are some interesting features to note. The weak downward trend in reflectance suggests the error models may diverge for reflectances beyond 0.5. However, nearly all data in the 0.2 to 0.5 reflectance range are desert matchups, and those cases may differ from ocean observations for a variety of reasons. The 550nm comparison in DOLP (cyan, 10b) also shows more scatter relative to 670 nm and 870 nm. These features may also be an artifact of a limited scene sample size, so a larger intercomparison study would be useful. It is also important to note that this comparison only includes matchups with VZA <= 35° to limit pointing knowledge, georegistration, and pixel projection errors in the comparison.

However, some errors may still exist. During ACEPOL, AirHARP did not have an on-board calibrator, mechanism of temperature regulation, or dry purge. If the field measurement was impacted by ascent-descent humidity changes, differences in temperature between the aircraft pod and the outside environment, or condensation of water and aggregation of ice particles on the front lens, these effects may be difficult to characterize. These may have asymmetric impacts on the data at different FOVs as well.

In Figure 9, we see some deviations between the AirHARP-RSP measurements, especially at larger scattering angles at 670nm and 870nm. This deviation may also be connected to georegistration at the widest angles, any unaccounted for misregistration between RSP and AirHARP, and/or interpolation at the AirHARP L1B stage. The HARP front lens distorts the ground projection by a factor of four at the furthest angles relative to nadir, so the amount of interpolation needed to fit the data on a common L1B grid is much more intense at far angles. This is complicated by "pitch surfing" of the ER-2. In several cases during ACEPOL, the ER-2 hit slight turbulence during flight, which briefly tilted the AirHARP

instrument off-nadir. Pitch surfing may grow the pixel projection at far angles and adds uncertainty in our interpolation of these angles in the gridding stage.

However, the overall structure of the RSP signal is reproduced by AirHARP instrument across two different scenes, a wide range of view angles, and relative to their mutual uncertainty. These results show the strength of our simple and efficient telecentric technique. The accuracy of this calibration is indirectly demonstrated in AirHARP Level 2 aerosol and cloud retrieval studies in Puthukuddy et al. (2020) and McBride et al. (2020), as well. Both studies use full-FOV datasets.

It is also important to note that cross-validation between instruments cannot determine which instrument is "more correct", only how well they both agree over a common range of angles, channels, and targets. The community anticipates a third-party intercomparison study in the future that compares the measurements of all ACEPOL polarimeters with each other, vector radiative transfer models, and other co-located satellite instruments.

## 5 Conclusions

The AirHARP calibration pipeline presented in this work exceeds the community requirement of 0.5% DOLP in the lab and reproduces the signal of natural targets relative to another co-located polarimeter. The telecentric calibration scheme is as effective as it is simple. It is also possible in a variety of environments: in space, where physical access is impossible, and during field campaigns, where time and access to the instrument is limited. If a flatfield measurement is done regularly and consistently, the performance of the entire FPA can be traced through a range of temperatures and humidity environments (on aircraft). The HARP2 instrument on the NASA PACE mission includes an internal calibrator to validate the full FOV performance throughout the life of the mission.

The telecentric technique can be used for vicarious calibration with field data alone, too. In the lab calibration, we used a rotating polarizer-sphere setup and pixels at the center of the lens to calculate the characteristic matrix. This is a special case. In general, any polarized target viewed from at least three different angles may provide enough information to trend the characteristic matrix. It is important that the target is viewed from significantly different geometry (optimally with views parallel and perpendicular to the solar plane, and/or at least three attack angles 60° apart). This achieves the highest discrimination

between polarization states (Tyo et al. 2006). Therefore, sunglint, cloudbow, dry lake, salt flat, aerosol plume, polar ice, and other natural targets can be excellent homogeneous and/or stable vicarious calibration targets. Measurements of these targets, combined with an internal flatfield measurement, may allow for an effective and efficient trending of the instrument.

710    The telecentric technique can also be used to cross-calibrate HARP against other polarimetric instruments. For example, a direct intercomparison of AirHARP and RSP could be used to derive a radiometric correction factor that could be applied to the characteristic matrix in Eq. (20). Because the radiometric *k-factor* applies to the entire matrix, a single co-located intercomparison between like instruments is enough to correct the measurement. Using co-located instruments in this way also transfers

715   their uncertainty in geolocation, measurement accuracy, and pointing. Nevertheless, it is invaluable over ill-modeled targets and/or validating against solar or lunar views. The HARP science team is currently evaluating how this telecentric technique can improve the in-flight calibration of AirHARP and HARP CubeSat data. We anticipate these methods will be applied to and expanded with HARP2 in 2024 and beyond.

## 6 Appendix

The RSP error model is provided in Knobelspiesse (2015). The overall error in reflectance and DOLP is described below:

$$\sigma_\rho^2 = \left(\frac{r^2\sigma_{floor}}{\mu_s}\right)^2 + \frac{a\,R_I r^2}{\mu_s} + \frac{\sigma_{lnK}^2 R_P^2}{16} + \sigma_{a_c}^2 R_I^2 \tag{22}$$

$$\sigma_{DOLP}^2(noise) = 4\left(1 + \frac{DOLP^2}{2}\right)\left(\frac{r^2\sigma_{floor}}{\mu_s R_I}\right)^2 + 2\left(1 - \frac{DOLP^2}{2}\right)\left(\frac{a\,r^2}{\mu_s R_I}\right) \tag{23}$$

$$\sigma_{DOLP}^2(cal) = \frac{\sigma_{lnK}^2}{2}\left[1 - DOLP^2 + \frac{DOLP^4}{2}\left(1 - \frac{1}{2}\sin^2 4\chi\right)\right] + \sigma_{lna}^2 DOLP^2 \tag{24}$$

$$\sigma_{DOLP}^2 = \sigma_{DOLP}^2(noise) + \sigma_{DOLP}^2(cal) \tag{25}$$

Several parameters are prescribed, based on Knobelspiesse (2015):

- Solar distance in AU, r: 1
- Noise floor, $\sigma_{floor}$ (x $10^{-5}$): 2.5 (550 nm), 2.2 (670 nm), and 2.0 (865 nm)
- Shot noise parameter, $a$ (x $10^{-9}$): 4.5 (550 nm), 3.7 (670 nm), 3.7 (865 nm)
- Relative gain coefficient cal uncertainty, $\sigma_{lnK}$: 0.005
- Absolute radiometric uncertainty, $\sigma_{a_c}$: 0.03
- Polarimetric characterization uncertainty, $\sigma_{lna}$: 0.001

Other parameters are given in the field datasets and are a function of observational geometry and Earth scene:

- Cosine of the solar zenith angle, $\mu_s$
- Intensity reflectance, $R_I$

- Polarized reflectance, $R_P$
- Degree of Linear Polarization, $DOLP$

Finally, the RSP DOLP uncertainty depends on the angle of polarization, $\chi$, in Eq. (24). In a sensitivity study with the above parameters and field data, we found that the intercomparison with AirHARP did not vary meaningfully when $\chi$ varied between 0 and 180°. Therefore, $\sin^2 4\chi$ was set to its expectation value, 0.5, which represents any angle $\chi = (45n + 11.25)\,°$ for $n$ in $\mathbb{Z}$.

The error model for AirHARP follow detector noises and systematics all the way to the Stokes parameters via uses Eqs. (18) and (19). Using Eq. (19) with i = 1 and re-arranging the numerator, we show the intensity (or reflectance, via conversion ) calibration and noise uncertainty:

$$\left(\frac{\sigma_I}{I}\right)^2 = \frac{\sum_{j=1}^{3} DN_{\text{det }j}^{*2}\left[\left(k\,\sigma_{C_{1j}}\right)^2 + \left(C_{1j}\,\sigma_k\right)^2\right] + \left(k\,C_{1j}\,\sigma_{DN_{\text{det }j}^*}\right)^2}{\left(\sum_{j=1}^{3} k\,C_{1j} DN_{\text{det }j}^*\right)^2},$$

(26)

From Table 2b (AirHARP 670nm), the matrix element error $\sigma_{C_{1j}}$ is comparable for all elements (~1e-3). The radiometric factor $k$ is 1.47e-5 W m$^{-2}$ nm$^{-1}$ sr$^{-1}$ ADU$^{-1}$, radiometric uncertainty $\sigma_k$ is 1e-3·$k$, the calibration matrix elements $C_{1j}$ are 1.020, -0.053, and 0.848, for j = [1,2,3] respectively. The $DN_{\text{det }j}^*$ is not part of the L1B product but can be retrieved using Eq. (18) in reverse. The $\sigma_{DN_{\text{det }j}^*}$ is a mixture of detector noises, calibration fit errors, pixel aggregation, and spatial variability in the scene. We typically

approximate this as the standard deviation of the reflectance factor superpixel in the L1B data, and is the main contributor to reflectance uncertainty. The total reflectance uncertainty in the L1B is thus:

765

$$\left(\frac{\Delta_L}{L}\right)^2 = (0.03)^2 + \left(\frac{\sigma_I}{I}\right)^2,\tag{27}$$

where the first term accounts for transfer radiometry error from integrating spheres, and the second term addresses superpixel SNR (using the intensity product, I, from the L1B granule). The

770 AirHARP DOLP uncertainty is a propagation from Eq. (7):

$$\sigma_{DOLP}^2 = \left(\frac{Q^2\sigma_Q^2 + U^2\sigma_U^2}{I^2(Q^2 + U^2)}\right) + \left(-\frac{\sqrt{Q^2 + U^2}}{I^2}\sigma_I\right)^2,\tag{28}$$

We can simplify using Eq. (7) again:

775

$$\Delta_{DOLP}^2 = (0.0025)^2 + \left(\frac{Q^2\sigma_Q^2 + U^2\sigma_U^2}{I^4 DOLP^2}\right) + \left(DOLP\frac{\sigma_I}{I}\right)^2,\tag{29}$$

where the 0.0025 is a systematic offset from the POLBOX measurements (Figure 8) and the last two terms are from Eq. (28). We anticipate using an expanded set of characterization measurements

780 from HARP2, detailed in Sienkiewicz et al. (2024, *in prep*), to develop a model that characterizes the entire FOV this year.

In all above equations, $\sigma$ is the standard deviation of the radiance in the AirHARP superpixel (for I, Q, or U as noted), which is weighted by the spatial mask.

785

**7 Code and data Availability**

NASA ACEPOL L1B datasets are available on https://www-air.larc.nasa.gov/cgi-bin/ArcView/acepol under "MARTINS J. VANDERLEI" (AirHARP) and "CAIRNS, BRIAN" (RSP). The specific AirHARP datasets used in this work are:

790
ACEPOL-AIRHARP-L1B_ER2_20171023201049_R2.h5 (Ocean 1)
ACEPOL-AIRHARP-L1B_ER2_20171023204956_R2.h5 (Ocean 2)
ACEPOL-AIRHARP-L1B_ER2_20171025172822_R2.h5 (Desert 1)
ACEPOL-AIRHARP-L1B_ER2_20171025175722_R2.h5 (Desert 2)
795 ACEPOL-AIRHARP-L1B_ER2_20171025182620_R2.h5 (Desert 3)
ACEPOL-AIRHARP-L1B_ER2_20171025185517_R2.h5 (Desert 4)
ACEPOL-AIRHARP-L1B_ER2_20171025192810_R2.h5 (Desert 5)

The RSP datasets used are:

800
ACEPOL-RSP2-L1B_ER2_20171023195451_R0.h5 (Ocean 1)
ACEPOL-RSP2-L1B_ER2_20171023204417_R0.h5 (Ocean 2)
ACEPOL-RSP2-L1B_ER2_20171025171811_R0.h5 (Desert 1)
ACEPOL-RSP2-L1B_ER2_20171025175031_R0.h5 (Desert 2)
805 ACEPOL-RSP2-L1B_ER2_20171025182124_R0.h5 (Desert 3)
ACEPOL-RSP2-L1B_ER2_20171025184712_R0.h5 (Desert 4)

RSP data from ACEPOL and other field campaigns is also publicly available at
810 https://data.giss.nasa.gov/pub/rsp/data/. The AirHARP pre-launch calibration data and codes are available
on request from the corresponding author.

## 7 Author contributions

BM developed the testing procedure, performed all lab and field calibrations for AirHARP, performed
the above analysis, and wrote this manuscript. BM and HMBJ led the AirHARP participation in the field
815 during the ACEPOL campaign. JVM is the principal investigator of the HARP missions. JVM, JDC, and
RFB led the engineering design and development, and supported AirHARP in the field with BM and
HMBJ. AP, XX, and NS provided intellectual contributions to several sections, from the perspective of
HARP CubeSat on-orbit data. BC is the principal investigator for the RSP instrument and data contact.
All co-authors made substantial edits and reviews to the manuscript.

## 8 Competing Interests

The authors declare no conflicts of interest.

## 9 Disclaimer

The statements contained within the research article are not the opinions of the funding agency or the U.S.
government, but reflect the author's opinions.

## 10 Acknowledgements

The authors thank the engineers and support staff at the UMBC Earth and Space Institute for their
continued support of the AirHARP, HARP CubeSat, and HARP2 missions. We also acknowledge the
ER-2 support personnel at the NASA Armstrong Flight Center during the NASA ACEPOL campaign,
especially the pilots who graciously operated AirHARP in targeting mode on many flights. We also thank

830 Jim Butler and John Cooper at the NASA GSFC Radiometric Calibration Facility for assisting with the many pre-launch characterizations of the HARP instruments. Finally, the authors also thank Pengwang Zhai, Martjin Smit, Kirk Knobelspiesse, Samuel Pellicori, Peter Dogoda, and Lorraine Remer for their contributions to and insights on this work over the years.

**11 Financial support**

835 Brent A. McBride received funding from the NASA Earth and Space Science Fellowship (grant no. 18-EARTH18R-40) under the NASA Science Mission Directorate. This study is supported and monitored by the National Oceanic and Atmospheric Administration – Cooperative Science Center for Earth System Sciences and Remote Sensing Technologies (NOAA-CESSRST) (grant no. NA16SEC4810008). Brent A. McBride has been supported by the City College of New York, the NOAA-CESSRT program, and

840 NOAA Office of Education (Educational Partnership Program). ACEPOL flight hours were funded in part by the SRON Netherlands Institute for Space Research and the NWO/NSO under project number ALW-GO/16-09.

**12 References**

845

ACEPOL Science Team: Aerosol Characterization from Polarimeter and Lidar Campaign, NASA Langley Atmospheric Science Data Center DAAC, https://doi.org/10.5067/SUBORBITAL/ACEPOL2017/DATA001, 2017.

850 Aldoretta, E., Angal, A., Twedt, K., Chen, H., Li, Y., Link, D., Mu, Q., Vermeesch, K., and Xiong, X.: The MODIS RSB calibration and look-up-table delivery process for collections 6 and 6.1. Proc. of SPIE, Earth Observing Systems XXV, 11501, https://doi.org/10.1117/12.2570785, 2020.

Boucher, O., Randall, D., Artaxo, P., Bretherton, C., Feingold, G., Forster, P., Kerminen, V. M., Kondo, 855 Y., Liao, H., Lohmann, U., Rasch, P., Satheesh, S. K., Sherwood, S., Stevens, B., Zhang, X. Y., Bala, G., Bellouin, N., Benedetti, A., Bony, S., Caldeira, K., Del Genio, A., Facchini, M. C., Flanner, M., Ghan, S., Granier, C., Hoose, C., Jones, A., Koike, M., Kravitz, B., Laken, B., Lebsock, M., Mahowald, N., Myhre, G., O'Dowd, C., Robock, A., Samset, B., Schmidt, H., Schulz, M., Stephens, G., Stier, P., Storelvmo, T., Winker, D., and Wyant, M.: Clouds and Aerosols, Climate Change 2013:

860     the Physical Science Basis, Cambridge University Press, Cambridge, United Kingdom and New York, NY, USA, 571–657, 2013.

Cairns, B., Russell, E. E., and Travis, L. D.: The research scanning polarimeter: Calibration and ground-based measurements, in: Proceedings of the Society of Photo-Optical Instrumentation Engineers
865     (Spie), Conference on Polarization – Measurement, Analysis, and Remote Sensing II, Denver, Co, WOS:000084180100021, 186–196, 1999.

Chowdhary, J., B. Cairns, F. Waquet, K. Knobelspiesse, M. Ottaviani, J. Redemann, L. Travis, and M. Mishchenko: Sensitivity of multiangle, multispectral polarimetric remote sensing over open oceans to
870     water-leaving radiance: Analyses of RSP data acquired during the MILAGRO campaign, Remote Sensing of Environment, 118, 284-308, doi:10.1016/j.rse.2011.11.003, 2012.

Cooper, J. and Butler, J.: NASA GSFC Code 618 Calibration Facility, available at: https://cl.gsfc.nasa.gov/ (last accessed on 28 September 2022), 2020.
875

Cox, C. and Munk, W: Measurement of the Roughness of the Sear Surface from Photographs of the Sun's Glitter, J. of the Opt. Soc. of Amer., 44, 838-850, 1954.

Diner, D. J., Xu, F., Garay, M. J., Martonchik, J. V., Rheingans, B. E., Geier, S., Davis, A., Hancock, B.
880     R., Jovanovic, V. M., Bull, M. A., Capraro, K., Chipman, R. A., and McClain, S. C.: The Airborne Multiangle SpectroPolarimetric Imager (AirMSPI): a new tool for aerosol and cloud remote sensing, Atmos. Meas. Tech., 6, 2007–2025, https://doi.org/10.5194/amt-6-2007-2013, 2013.

Diner, D. J., Boland, S. W., Brauer, M., Bruegge, C., Burke, K. A., Chipman, R., Girolamo, L. D.,
885     Garay, M. J., Hasheminassab, S., Hyer, E., Jerrett, M., Jovanovic, V., Kalashnikova, O. V., Liu, Y., Lyapustin, A. I., Martin, R. V., Nastan, A., Ostro, B. D., Ritz, B., Schwartz, J., Wang, J., and Xu, F.: Advances in multiangle satellite remote sensing of speciated airborne particulate matter and association with adverse health effects: from MISR to MAIA, J. Appl. Remote Sens., 12, 1–22, https://doi.org/10.1117/1.JRS.12.042603, 2018.
890

Dubovik, O., Li, Z. Q., Mishchenko, M. I., Tanre, D., Karol, Y., Bojkov, B., Cairns, B., Diner, D. J., Espinosa, W. R., Goloub, P., Gu, X. F., Hasekamp, O., Hong, J., Hou, W. Z., Knobelspiesse, K. D., Landgraf, J., Li, L., Litvinov, P., Liu, Y., Lopatin, A., Marbach, T., Maring, H., Martins, V., Meijer, Y., Milinevsky, G., Mukai, S., Parol, F., Qiao, Y. L., Remer, L., Rietjens, J., Sano, I., Stammes, P.,
895     Stamnes, S., Sun, X. B., Tabary, P., Travis, L. D., Waquet, F., Xu, F., Yan, C. X., and Yin, D. K.: Polarimetric remote sensing of atmospheric aerosols: Instruments, methodologies, results, and perspectives, J. Quant. Spectrosc. Ra., 224, 474–511, https://doi.org/10.1016/j.jqsrt.2018.11.024, 2019.

900  Fernandez-Borda, R., Waluschka, E., Pellicori, S., Martins, J. V., Ramos-Izquierdo, L., Cieslak, J. D., and Thompson, P.: Evaluation of the polarization properties of a Philips-type prism for the

construction of imaging polarimeters, in: Polarization Science and Remote Sensing IV, edited by: Shaw, J. A. and Tyo, J. S., Proceedings of SPIE, 7461, 2009.

905 Frouin, R. J., Franz, B. A., Ibrahim, A., Knobelspiesse, K., Ahmad, Z., Cairns, B., Chowdhary, J., Dierssen, H. M., Tan, J., Dubovik, O., Huang, X., Davis, A. B., Kalashnikova, O., Thompson, D. R., Remer, L. A., Boss, E., Coddington, O., Deschamps, P.-Y., Gao, B.-C., Gross, L., Hasekamp, O., Omar, A., Pelletier, B., Ramon, D., Steinmetz, F., and Zhai, P.-W.: Atmospheric Correction of Satellite Ocean-Color Imagery During the PACE Era, Front. Earth Sci., 7, 145, https://doi.org/10.3389/feart.2019.00145, 2019.

910

Gao, M., Zhai, P.-W., Franz, B. A., Knobelspiesse, K., Ibrahim, A., Cairns, B., Craig, S. E., Fu, G., Hasekamp, O., Hu, Y., and Werdell, P. J.: Inversion of multiangular polarimetric measurements from the ACEPOL campaign: an application of improving aerosol property and hyperspectral ocean color retrievals, Atmos. Meas. Tech., 13, 3939–3956, https://doi.org/10.5194/amt-13-3939-2020, 2020.

915

Hansen, J.E., and Travis, L.D.: Light scattering in planetary atmospheres. Space Sci. Rev., 16, 527-610, doi:10.1007/BF00168069, 1974.

Hasekamp, O. P. and Landgraf, J.: Retrieval of aerosol properties over land surfaces: capabilities of
920 multiple-viewing-angle intensity and polarization measurements, Appl. Optics, 46, 3332–3344, https://doi.org/10.1364/ao.46.003332, 2007.

Hasekamp, O. P., Fu, G. L., Rusli, S. P., Wu, L. H., Di Noia, A., de Brugh, J. A., Landgraf, J., Smit, J. M., Rietjens, J., and van Amerongen, A.: Aerosol measurements by SPEXone on the NASA PACE mission: expected retrieval capabilities, J. Quant. Spectrosc. Ra., 227, 170–
925 184, https://doi.org/10.1016/j.jqsrt.2019.02.006, 2019.

Jackson, J. D.: Classical Electrodynamics, available at: https://www.google.com/books/edition/_/8qHCZjJHRUgC?hl=en&sa=X&ved=2ahUKEwiwh43No6XyAhUBUzUKHSlfBngQ7_IDMBR6BAgKEAM (last access: 9 August 2021), 2012.

930 Kliger, D. S, Lewis, J. W., and Randall, C. E.: Polarized Light in Optics and Spectroscopy. Boston: Academic Press, 1990.

Knobelspiesse, K., Cairns, B., Mishchenko, M., Chowdhary, J., Tsigaridis, K., van Diedenhoven, B., Martin, W., Ottaviani, M., and Alexandrov, M.: Analysis of fine-mode aerosol retrieval capabilities
935 by different passive remote sensing instrument designs, Opt. Express, 20, 21457–21484, https://doi.org/10.1364/OE.20.021457, 2012.

Knobelspiesse, K., Tan, Q., Bruegge, C., Cairns, B., Chowdhary, J., van Diedenhoven, B., Diner, D., Ferrare, R., van Harten, G., Jovanovic, V., Ottaviani, M., Redemann, J., Seidel, F., and Sinclair, K.:

Intercomparison of airborne multi-angle polarimeter observations from the Polarimeter Definition Experiment, Appl. Optics, 58, 650–669, https://doi.org/10.1364/ao.58.000650, 2019.

Knobelspiesse, K., Barbosa, H. M. J., Bradley, C., Bruegge, C., Cairns, B., Chen, G., Chowdhary, J., Cook, A., Di Noia, A., van Diedenhoven, B., Diner, D. J., Ferrare, R., Fu, G., Gao, M., Garay, M., Hair, J., Harper, D., van Harten, G., Hasekamp, O., Helmlinger, M., Hostetler, C., Kalashnikova, O., Kupchock, A., Longo De Freitas, K., Maring, H., Martins, J. V., McBride, B., McGill, M., Norlin, K., Puthukkudy, A., Rheingans, B., Rietjens, J., Seidel, F. C., da Silva, A., Smit, M., Stamnes, S., Tan, Q., Val, S., Wasilewski, A., Xu, F., Xu, X., and Yorks, J.: The Aerosol Characterization from Polarimeter and Lidar (ACEPOL) airborne field campaign, Earth Syst. Sci. Data., https://doi.org/10.5194/essd-2020-76, 2020.

Li Z., Li, K., Li, L., Xu, H., Xie, Y., Ma, Y. ,Li, D., Goloub, P., Yuan, Y., and Zheng, X: Calibration of the degree of linear polarization measurements of the polarized sun-sky radiometer based on the POLBOX system, Appl. Opt., 57, 1011-1018, https://doi.org/10.1364/AO.57.001011, 2018.

Martins, J. V., Fernandez-Borda, R., McBride, B., Remer, L., and Barbosa, H. M. J.: THE HARP HYPERANGULAR IMAGING POLARIMETER AND THE NEED FOR SMALL SATELLITE PAYLOADS WITH HIGH SCIENCE PAYOFF FOR EARTH SCIENCE REMOTE SENSING, IGARSS 2018 – 2018 IEEE International Geoscience and Remote Sensing Symposium, 22–27 July 2018 in Valencia, Spain, 6304–6307, 2018.

McBride, B. A., Martins, J. V., Barbosa, H. M. J., Birmingham, W., and Remer, L. A.: Spatial distribution of cloud droplet size properties from Airborne Hyper-Angular Rainbow Polarimeter (AirHARP) measurements, Atmos. Meas. Tech., 13, 1777–1796, https://doi.org/10.5194/amt-13-1777-2020, 2020.

McBride, B. A., Martins, J. V., Puthukuddy, A., Xu, X., Fernandez-Borda, R., Barbosa, H. M. J., Hasekamp, O, and Remer, L. A.: The Hyper-Angular Rainbow Polarimeter-2 (HARP2): a wide FOV

polarimetric imager for high resolution spatial and angular characterization of aerosol and cloud
970    microphysics, in: Proceedings of the 70th International Astronautical Congress, 2019.

McClain, S. C., Bartlett, C. L., Pezzaniti, J. L., and Chipman, R. A.: Depolarization measurements of an integrating sphere, in: Proceedings of SPIE, 1994.

975    Mishchenko, M. I., Cairns, B., Hansen, J. E., Travis, L. D., Burg, R., Kaufman, Y. J., Vanderlei Martins, J., and Shettle, E. P.: Monitoring of aerosol forcing of climate from space: analysis of measurement requirements, J. Quant. Spectrosc. Ra., 88, 149–161, 2004.

Knobelspiesse, K: Research Scanning Polarimeter Uncertainty Model, available at:
980    https://airbornescience.nasa.gov/sites/default/files/documents/rsp_unc.pdf (last access 9 Aug 2021), 2015.

NASA, AtmOS Polarimeter Instrumentation, available at:
https://aos.gsfc.nasa.gov/docs/ATMOS_Polarimeter_210602_final_revised.pdf (last accessed on 28
985    September 2022), 2021.

NASA, PACE: Pre-Aerosol,Clouds, and ocean Ecosystem (PACE) Mission Science Definition Team Report, available at: https://pace.oceansciences.org/docs/PACE_TM2018-219027_Vol_2.pdf (last access: 9 August 2021), 2018.
990
NASA, Polarimetry in the PACE Mission, Science Team Consensus Document, available at:
https://pace.oceansciences.org/docs/PACE_polarimetry_final.pdf (last accessed 28 September 2022), 2015.

995    NREL, 2000 ASTM Standard Extraterrestrial Spectrum Reference E-490-00, available at:
https://www.nrel.gov/grid/solar-resource/spectra-astm-e490.html (last accessed on 28 September 2022), 2000.

Pörtge, V., Kölling, T., Weber, A., Volkmer, L., Emde, C., Zinner, T., Forster, L., and Mayer, B.: High-
1000    spatial-resolution retrieval of cloud droplet size distribution from polarized observations of the cloudbow, Atmos. Meas. Tech., 16, 645–667, https://doi.org/10.5194/amt-16-645-2023, 2023.

Puthukkudy, A., Martins, J. V., Remer, L. A., Xu, X., Dubovik, O., Litvinov, P., McBride, B., Burton, S., and Barbosa, H. M. J.: Retrieval of aerosol properties from Airborne Hyper Angular Rainbow
1005    Polarimeter (AirHARP) observations during ACEPOL 2017, Atmos. Meas. Tech., https://doi.org/10.5194/amt-2020-64, 2020.

Rietjens, J., Campo, J., Chanumolu, A., Smit, M., Nalla, R., Fernandez, C., Dingjan, J., van Amerongen, A., and Hasekamp, O.: Expected performance and error analysis for SPEXone, a multi-angle

1010     channeled spectropolarimeter for the NASA PACE mission. in: Polarization Science and Remote
        Sensing IX 34 -- 47) SPIE., 2019.

        Remer, L. A., Knobelspiesse, K., Zhai, P. W., Xu, F., Kalashnikova, O. V., Chowdhary, J., Hasekamp,
        O., Dubovik, O., Wu, L. H., Ahmad, Z., Boss, E., Cairns, B., Coddington, O., Davis, A. B., Dierssen,
1015    H. M., Diner, D. J., Franz, B., Frouin, R., Gao, B. C., Ibrahim, A., Levy, R. C., Martins, J. V., Omar,
        A. H., and Torres, O.: Retrieving Aerosol Characteristics From the PACE Mission, Part 2: Multi-
        Angle and Polarimetry, Front. Env. Sci., 7, 94, https://doi.org/10.3389/fenvs.2019.00094, 2019.

        Semiconductor Components Industries, LLC. KAI-04070 2048 (H) x 2048 (V) Interline CCD Image
1020    Sensor. https://www.imperx.com/wp-content/uploads/2017/08/KAI-04070-D.pdf [Last accessed 15 May
        2024].

        Schott, J. R.: Fundamentals of Polarimetric Remote Sensing, Society of Photo Optical, available
        at: https://books.google.com/books?id=-2V0gAJ3aG4C (last access: 9 August 2021), 2009.
1025

        Sienkiewicz, N., Martins, J. V., McBride, B.A., Xu. X., Puthukkudy, A., Smith, R., and Fernandez-
        Borda, R.: HARP2 Pre-Launch Calibration Overview: The Effects of a Wide Field of View. In prep
        for Atmospheric Measurement Techniques, 2024.

1030    Sinclair, K., van Diedenhoven, B., Cairns, B., Alexandrov, M., Dzambo, A. M., & L'Ecuyer,
        T.: Inference of precipitation in warm stratiform clouds using remotely sensed observations of the
        cloud top droplet size distribution. Geo. Res. Lett., 48, https://doi.org/10.1029/2021GL092547, 2021.

        Smit, J. M., Rietjens, J. H. H., van Harten, G., Noia, A. D., Laauwen, W., Rheingans, B. E., Diner, D. J.,
1035    Cairns, B., Wasilewski, A., Knobelspiesse, K. D., Ferrare, R., and Hasekamp, O. P.: SPEX airborne
        spectropolarimeter calibration and performance, Appl. Optics, 58, 5695–
        5719, https://doi.org/10.1364/AO.58.005695, 2019.

        Stamnes, S., Hostetler, C., Ferrare, R., Burton, S., Liu, X., Hair, J., Hu, Y., Wasilewski, A., Martin, W.,
1040    van Diedenhoven, B., Chowdhary, J., Cetinić, I., Berg, L. K., Stamnes, K., and Cairns, B.:
        Simultaneous polarimeter retrievals of microphysical aerosol and ocean color parameters from the
        "MAPP" algorithm with comparison to high-spectral-resolution lidar aerosol and ocean products,
        Appl. Optics, 57, 2394–2413, https://doi.org/10.1364/AO.57.002394, 2018.

1045    Stanier, C. O., Pierce, R. B., Abdi-Oskouei, M., Adelman, Z. E., Al-Saadi, J., Alwe, H. D., Bertram, T.
        H., Carmichael, G. R., Christiansen, M. B., Cleary, P. A., Czarnetzki, A. C., Dickens, A. F., Fuoco, M.
        A., Hughes, D. D., Hupy, J. P., Janz, S. J., Judd, L. M., Kenski, D., Kowalewski, M. G., Long, R. W.,
        Millet, D. B., Novak, G., Roozitalab, B., Shaw, S. L., Stone, E. A., Szykman, J., Valin, L., Vermeuel,
        M., Wagner, T. J., Whitehill, A. R., & Williams, D. J. (2021). Overview of the Lake Michigan Ozone
1050    Study 2017. Bulletin of the American Meteorological Society, 102, 12, E2207-E2225.
        https://doi.org/10.1175/BAMS-D-20-0061.1, 2021

Tyo, J., Goldstein, D., Chenault, D., and Shaw, J.: Review of passive imaging polarimetry for remote sensing applications. Appl. Opt., 45, 5453-5469, https://doi.org/10.1364/AO.45.005453, 2006.

van Diedenhoven, B., Cairns, B., Fridlind, A. M., Ackerman, A. S., and Garrett, T. J.: Remote sensing of ice crystal asymmetry parameter using multi-directional polarization measurements – Part 2: Application to the Research Scanning Polarimeter, Atmos. Chem. Phys., 13, 3185–3203, https://doi.org/10.5194/acp-13-3185-2013, 2013.

van Harten, G., Diner, D. J., Daugherty, B. J. S., Rheingans, B. E., Bull, M. A., Seidel, F. C., Chipman, R. A., Cairns, B., Wasilewski, A. P., and Knobelspiesse, K. D.: Calibration and validation of Airborne Multiangle SpectroPolarimetric Imager (AirMSPI) polarization measurements, Appl. Optics, 57, 4499–4513, https://doi.org/10.1364/ao.57.004499, 2018.

van Harten, G. and Diner, D. J.: AirMSPI radiometric/polarimetric uncertainties, available at https://airbornescience.nasa.gov/sites/default/files/documents/AirMSPI_uncertainty_model_15Aug2017.pdf (last accessed on 28 September 2022), 2015.

Weber, A., Kölling, T., Pörtge, V., Baumgartner, A., Rammeloo, C., Zinner, T., and Mayer, B.: Polarization upgrade of specMACS: calibration and characterization of the 2D RGB polarization-resolving cameras, Atmos. Meas. Tech., 17, 1419–1439, https://doi.org/10.5194/amt-17-1419-2024, 2024.

Werdell, P. J., Behrenfeld, M. J., Bontempi, P. S., Boss, E., Cairns, B., Davis, G. T., Franz, B. A., Gliese, U. B., Gorman, E. T., Hasekamp, O., Knobelspiesse, K. D., Mannino, A., Martins, J. V., McClain, C. R., Meister, G., and Remer, L. A.: The Plankton, Aerosol, Cloud, Ocean Ecosystem Mission: Status, Science, Advances, B. Am. Meteorol. Soc., 100, 1775–1794, https://doi.org/10.1175/BAMS-D-18-0056.1, 2019.

Wu, L., Hasekamp, O., van Diedenhoven, B., and Cairns, B.: Aerosol retrieval from multiangle, multispectral photopolarimetric measurements: importance of spectral range and angular resolution, Atmos. Meas. Tech., 8, 2625–2638, https://doi.org/10.5194/amt-8-2625-2015, 2015.

## 11 Tables

Table 1. Specifications of the AirHARP detectors

| | |
|---|---|
| Number of Active Pixels | 2048x2048 |
| Pixel Size | 7.4 x 7.4 µm |
| Quantum Efficiency (440,550,670,870 nm) | 0.52, 0.50, 0.31, 0.07 |
| RMS Read Noise | 12 e⁻ |
| Dark Current | 3 e⁻/s |
| Operational Integration Time | 20 ms |

Table 2a. Example characteristic matrix elements, $C_{ij}$, for the 670nm AirHARP band, via Eq. (12).

| $C_{ij}$ | j = 1 | j = 2 | j = 3 |
|---|---|---|---|
| i = 1 | $1.020 \pm 0.001$ | $-0.053 \pm 0.002$ | $0.848 \pm <0.001$ |
| i = 2 | $-0.843 \pm 0.001$ | $-0.309 \pm 0.001$ | $0.938 \pm <0.001$ |
| i = 3 | $-1.257 \pm <0.001$ | $2.230 \pm 0.001$ | $-0.689 \pm <0.001$ |

Table 2b. Example of instrument-relative parameters for 670nm AirHARP band, via Eq. (13).

| | f (%/100) | g (%/100) | $\beta(°)$ |
|---|---|---|---|
| Sensor A ($\theta_A = 0°$) | $0.501 \pm <0.001$ | $0.994 \pm 0.002$ | $-3.261 \pm 0.060$ |
| Sensor B ($\theta_B = 45°$) | $0.471 \pm <0.001$ | $0.970 \pm 0.002$ | $-6.115 \pm 0.048$ |
| Sensor C ($\theta_C = 90°$) | $0.605 \pm <0.001$ | $0.985 \pm 0.003$ | $-4.608 \pm 0.060$ |

Table 3. Derived AirHARP parameters from spectral response analysis

| Nominal Channel (nm) | Center (nm) | Bandwidth (nm) | $F_0$ (W m$^{-2}$ nm$^{-1}$) |
|---|---|---|---|
| 440nm | 441.4 | 15.7 | 1.855 |
| 550nm | 549.8 | 12.4 | 1.873 |
| 670nm | 669.4 | 18.1 | 1.534 |
| 870nm | 867.8 | 38.7 | 0.965 |

**12 Figures and Captions**

1100

(b) Payload (1.5U)

(a) HARP CubeSat (3U)

(c) Payload to scale
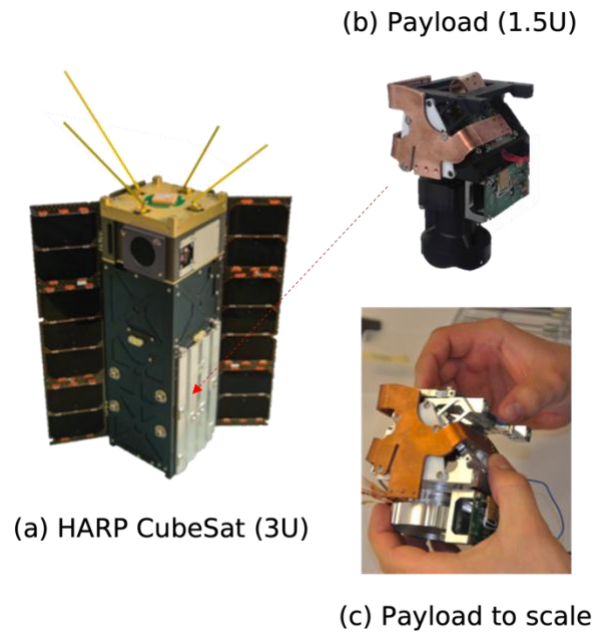
**Figure 1.** AirHARP is an aircraft demonstration of the HARP CubeSat (a), a standalone 3U spacecraft, which carries the same the 1.5U instrument (b) in the lower half of the housing. The payload can fit in the palm of a human hand (c).

1105
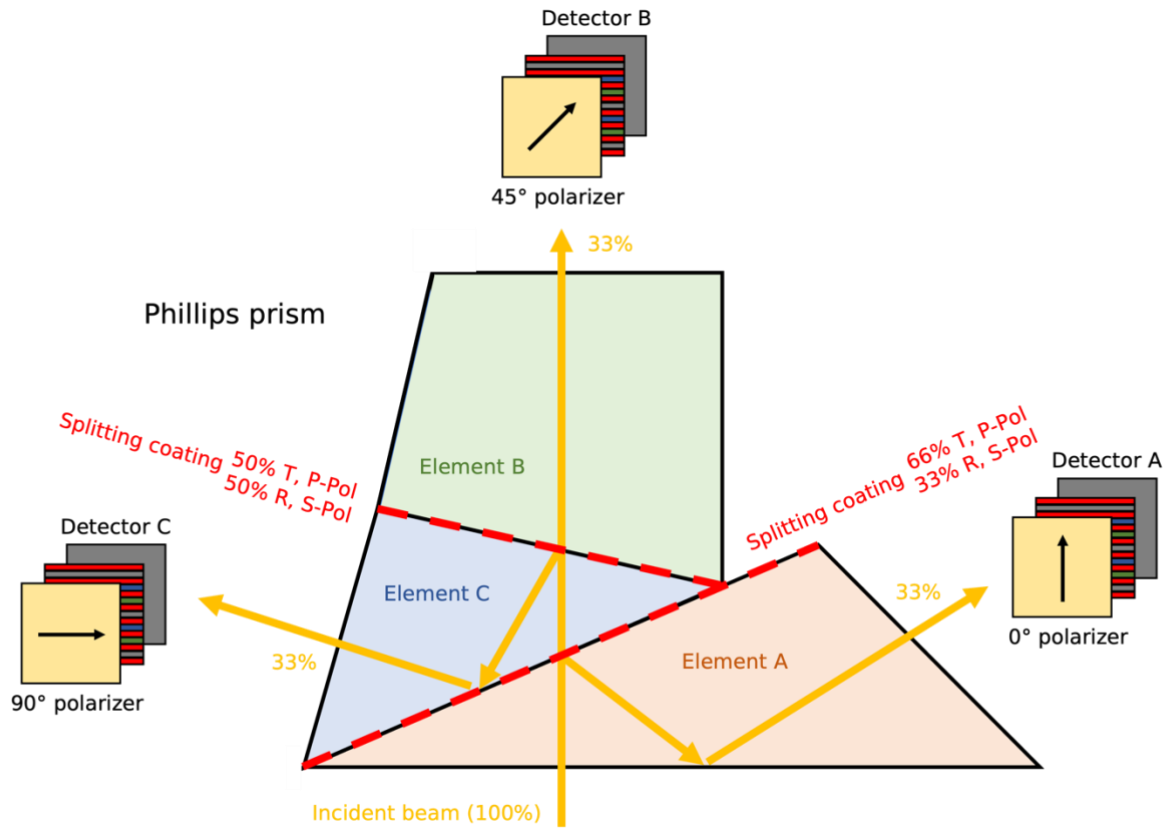
**Figure 2.** The Phillips prism is made of three elements: A, B, and C. Two splitting coatings split polarization states by transmission (T) and reflection (R). The coatings ensure that each HARP detector sees ~33% of the incident beam. The angle of the detector polarizer boosts the polarization efficiency of the prism along that light path. The light encounters the polarizer, stripe filter, then the detector FPA.
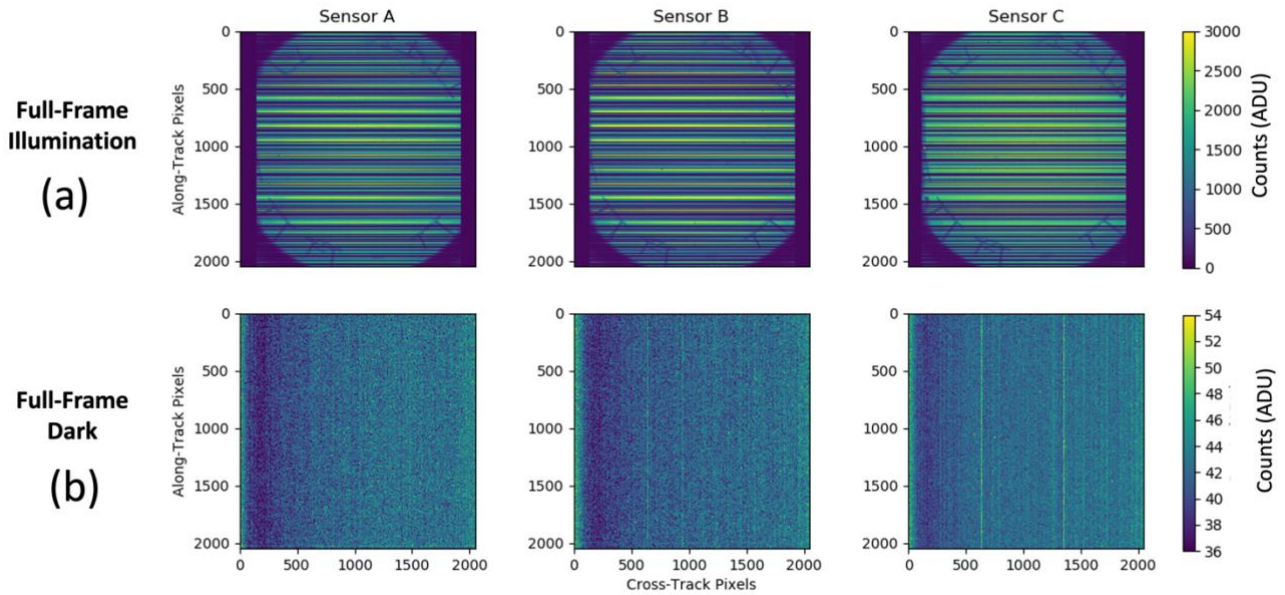
**Figure 3.** AirHARP captures a full-field raw image in each detector of the aperture of the NASA GSFC "Grande"
1115 integrating sphere (a) and a dark capture with the lens cap on (b). The dark shown here can be normalized and used
as a template for any live data capture.
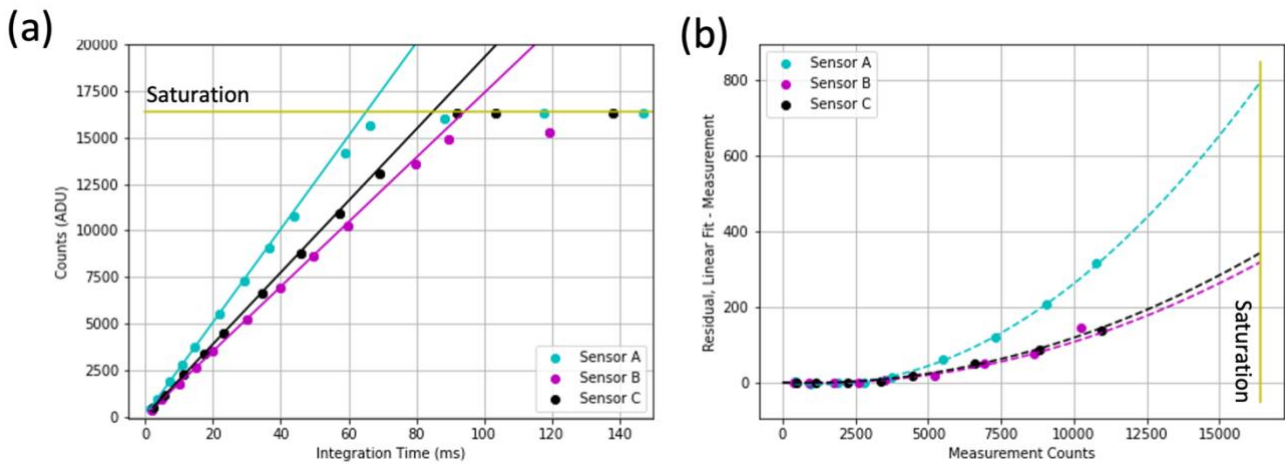
1120 **Figure 4.** AirHARP detector integration time is varied while imaging a stable light source (670nm channel shown).
The counts in the linear regime (<3000 ADU) are fit in (a) for all sensors. This linear fit is compared to the entire
dataset, and the residual is fit to a three parameter quadratic (b), which can now correct any raw measurement >
3000 ADU.
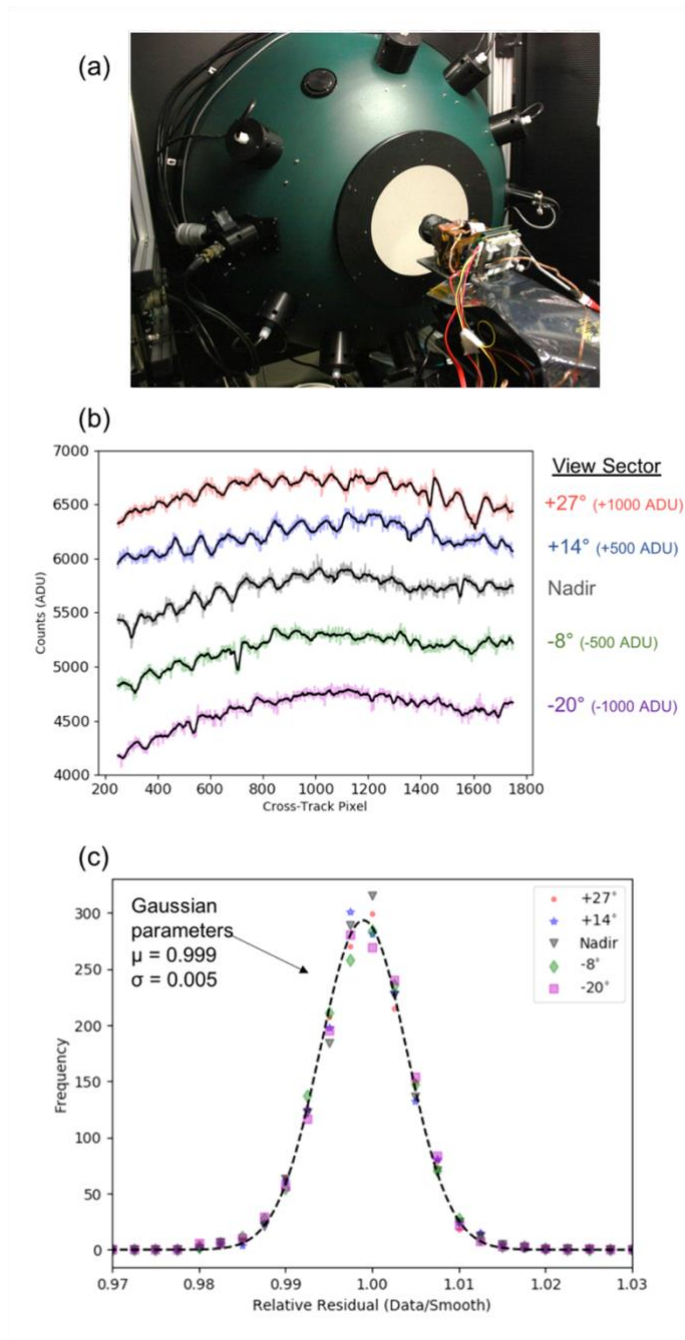
1125

**Figure 5.** The flatfield is performed by submerging the wide field front lens into the aperture of an integrating sphere (a). This creates a full-field image similar to Figure 3a. In (b), the cross-track signal for several detector rows (colored data) is smoothed (black curves). After Eq. (3) is applied, only the pixel-to-pixel variations due to noise remains, which is normally distributed within 0.5% across the FOV. Data in (b) and (c) shown for AirHARP
1130    670nm.

1135
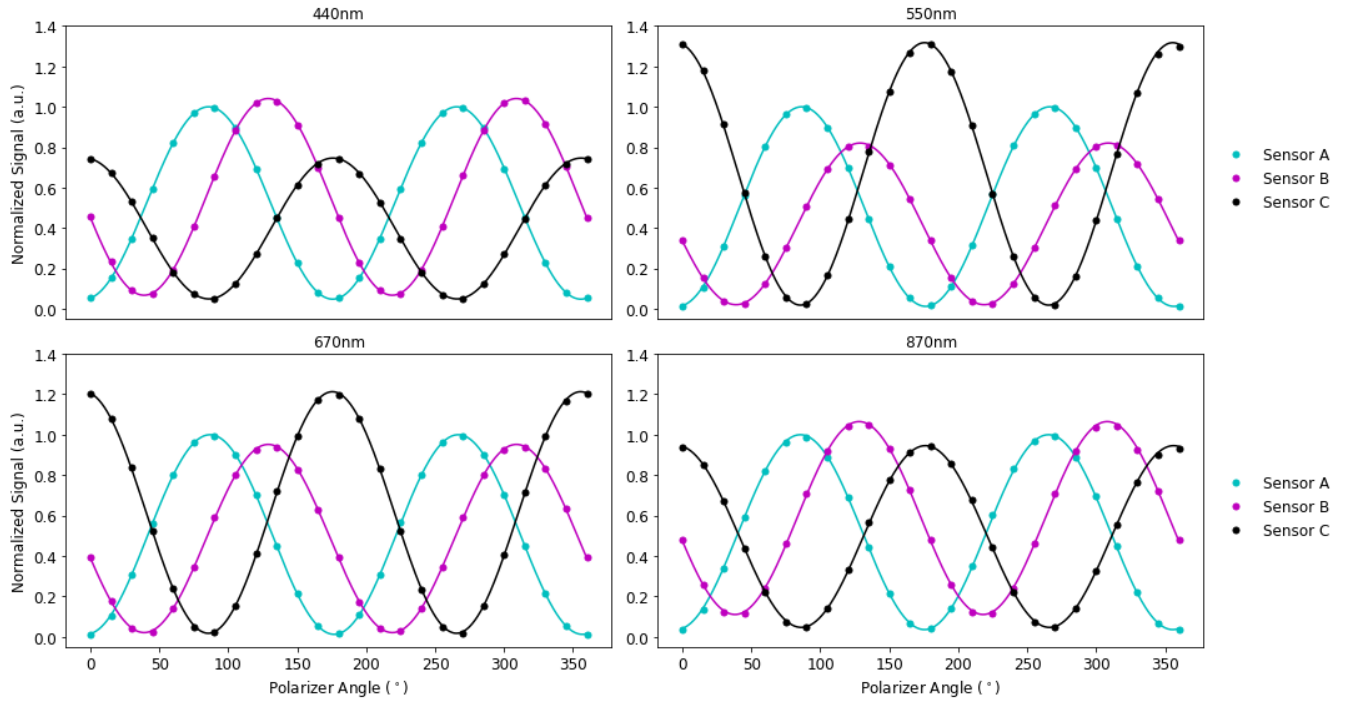
**Figure 6.** Malus curves for each of the four AirHARP channels. Each plot corresponds to an AirHARP channel,
1140 with data from Sensors A (cyan), B (magenta), and C (black) fit to Eq. (12) (solid lines). The data and fits are
normalized to the Sensor A maximum and represent the closest 4x10 nadir pixel bin, in each channel, to the
AirHARP optical axis. Note the polarizer rotation angle is offset by -90° as shown.
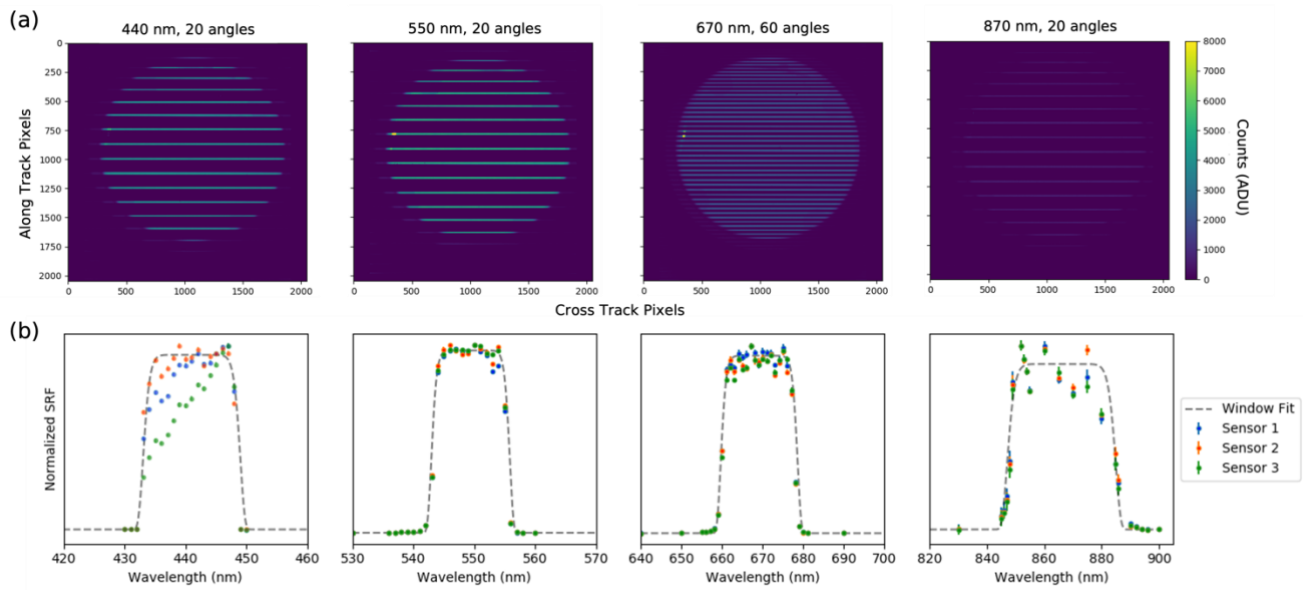
1145

**Figure 7.** Examples of AirHARP images taken at different in-band Ekpsla wavelengths to show the distribution of illuminated stripes (a). The Ekspla power was weakest in the near-infrared, as evidenced in the 870 nm example (a, right). The AirHARP SRF for the three sensors and the super-Gaussian SRF fit (gray) is shown in (b). The panels in (b) correspond to the panels in (a). All data shown in (b) is normalized to 1 for each channel and sensor
1150    individually.
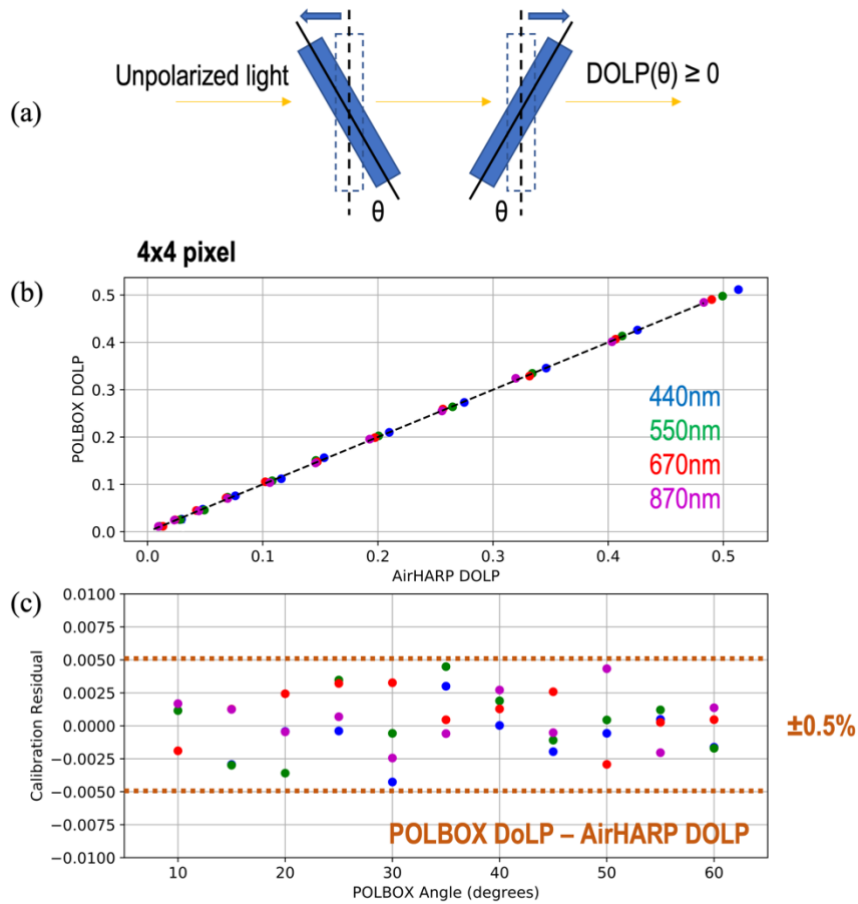
**Figure 8.** The POLBOX system generates partial polarization by rotating two glass blades (a). When comparing the DOLP theory to AirHARP measurement in all channels (b), we see AirHARP reproduces the entire POLBOX range within ± 0.5% DOLP (c). The lamp reflectance for this measurement was > 0.09 in all channels.
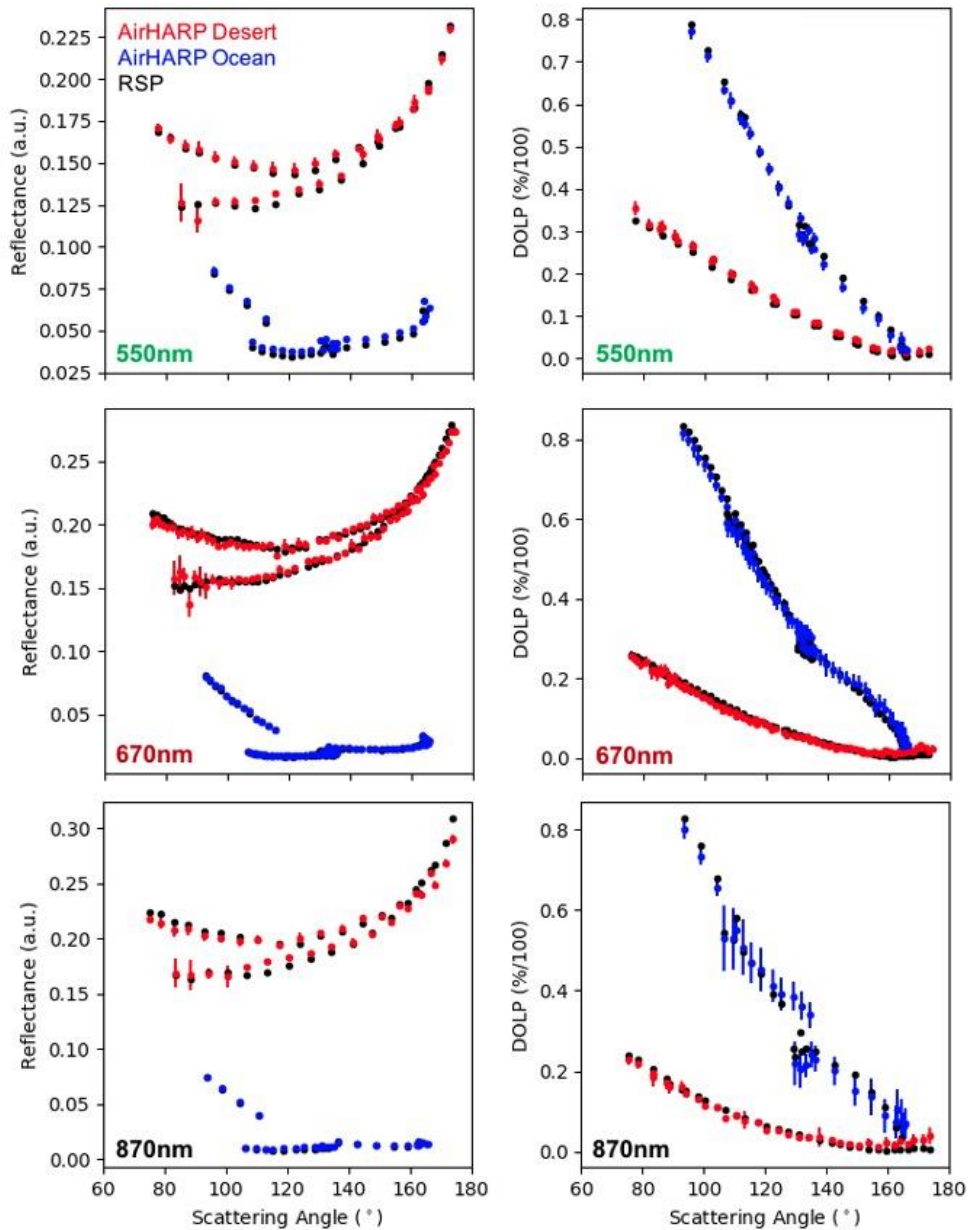
**Figure 9.** Multi-angle, interpolated matchups between AirHARP and RSP for ACEPOL targets. Reflectance factor
(left column) and DOLP (right column) are compared for three compatible spectral channels: 550nm (top), 670nm
(middle), and 870nm (bottom). AirHARP data in the colors and RSP is black, with red signifying Desert 1 and 2
cases and blue data as Ocean 1 and 2 cases. Error bars on the AirHARP data represent the standard deviation of the
superpixel bin.

1160

1165
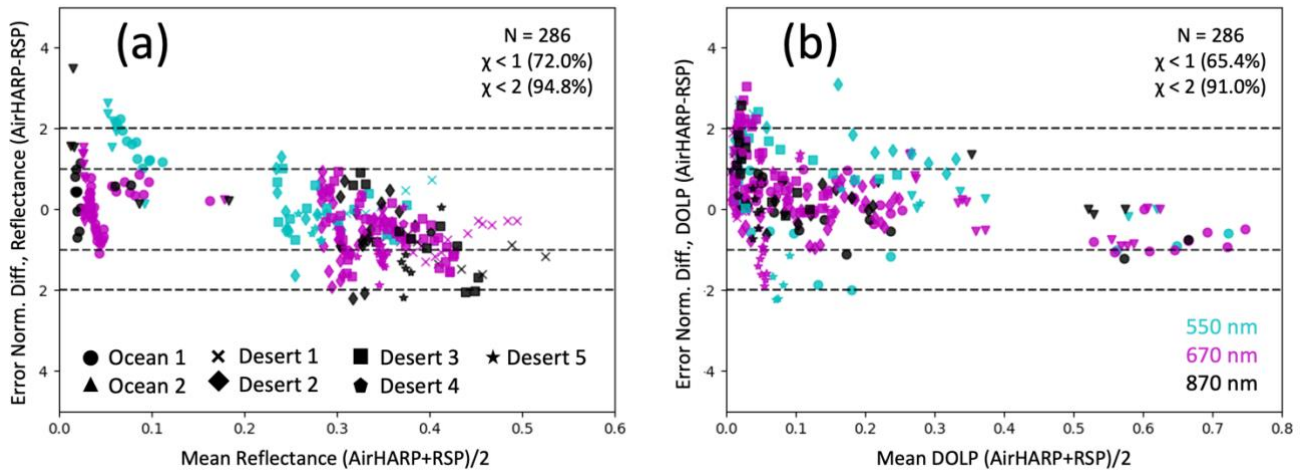
**Figure 10.** Error-normalized difference comparison between AirHARP and RSP reflectance (a) and DOLP (b) for 550nm (cyan), 670nm (magenta), and 870nm (black) data over two ocean and five desert ACEPOL cases (markers). The dashed black lines represent boundaries where the residuals are 1 and 2 times the mutual uncertainty of the AirHARP and RSP error models. All data shown represent co-located angular matchups within 1° VZA and 5° VAA. Only data with VZA >= 35° shown.

1170